3D numerical simulation and experimental investigation of pure tin solidification under natural and forced convection

Ibrahim Sari, Lakhdar Hachani, Abdellah Kharicha, Yves Fautrelle, Benjamin Pichat, Kader Zaidat

Version of Record: https://www.sciencedirect.com/science/article/pii/S1290072921000673
Manuscript_3e799901806aac24415ce9a672d44b47

3D Numerical Simulation and Experimental Investigation of Pure Tin Solidification Under Natural and Forced Convection

Ibrahim SARI[a], Lakhdar HACHANI[a], Abdellah KHARICHA[c], Yves FAUTRELLE[b], B. Pichat[b], Kader ZAIDAT[b,*]

[a] *Laboratoire Physique des Matériaux, Université Amar Telidji-Laghouat, Route de Ghardaia, BP 37G, Laghouat, Algeria.*

[b] *Univ. Grenoble Alpes, Grenoble-INP, CNRS, SIMaP, F-38000 Grenoble, France.*

[c] *Christian-Doppler Laboratory for Metallurgical Applications of Magnetohydrodynamics. Montanuniversitaet of Leoben, Franz-Josef-Str. 18, A-8700 Leoben, Austria.*

**kader.zaidat@grenoble-inp.fr*

Abstract

The numerical simulation of the horizontal solidification of pure tin under natural convection and under forced convection induced by Electromagnetic Stirring (EMS) is presented and compared with experimental results obtained by the 'AFRODITE' benchmark setup, described in several previous publications [6-10]. The experiment consists in solidifying a rectangular ingot (100×10×60 mm) using two lateral heat exchangers which allow the application of a controlled horizontal temperature difference. The experimental temperature difference between the two lateral sides of the sample DT = 40 K and the cooling rate CR = -0.03K/s. Under these conditions the solidification front is planar throughout the experiment. Enthalpy formulation based on fixed-grid techniques is used for the numerical simulations of the phase-change problems, accounting for buoyancy convection and forced convection created by Lorentz forces generated by an external Travelling Magnetic Field (TMF). The temperature distribution obtained by numerical simulation is demonstrated to effectively reproduce the temperature maps obtained from the experimental measurements. The proposed 3D numerical model has demonstrated its effectiveness in predicting the effect of EM stirring on the solidification process in terms of thermal field, dynamic field and the shape and localization of the solidification front.

Keywords *Solidification; natural/forced convection; 3D model; phase change; Electromagnetic Stirring; Lorentz force.*

1. Introduction

Over the last few decades, many researchers have been interested in the solidification process because of its role in major pathways to producing materials, especially metals and alloys. The conditions for the transformation from liquid to solid (phase change process), such as the temperature gradient and the growth rate, vary from process to process and also within a process as a function of time and space. For this reason we need numerical simulation when the simulated problems are complex, in order to obtain more significant results. This is especially the case for the solidification of metallic liquids in convective conditions, which can be seen as a complex problem. An example is the case of a rectangular ingot, given the simplicity of both the numerical resolution and the experimental characterization. The work

presented in this paper is rooted in the experimental work by Hebditch and Hunt [1], in which the mechanism of action of natural convection on macrosegregation formation was studied. By promoting horizontal solidification (perpendicular to gravity) of tin alloys displaying large density variations during solidification, significant macrosegregation was observed. The experiment was designed as quasi-2D and has been used as a basis for many numerical studies, including benchmark problems [2, 3] and studies of the impact of microsegregation modelling [4]. Hachani *et al.* [5] report binary tin alloy solidification experimental work and show that, though regular patterns are expected in the solidified ingot mesostructure, significant statistical variations in their location are also to be expected. This is a strong new argument in favour of the development of models using statistical approaches. The directional solidification benchmark setup AFRODITE, which is the subject of this paper, was proposed as a 'quasi-2D' experiment by Fautrelle and co-workers [6–10]. The solidified samples are 10 cm long, 6 cm high and only 1 cm thick. A very tricky issue in comparing computational models with this form of experimental study is the need to introduce adequate practical boundary conditions for the problem of heat transfer [11, 12]. Boussaa *et al.* [9, 10] validated a model based on a two-phase volume-averaged technique using Sn-3wt % Pb alloy experimental results. They concluded that the 2D calculation approach overestimates the velocity field by a factor of 1.5, leading to inconsistency with respect to the experimental results. They also found that the damping effect of the lateral walls taken into account in the 3D models provides significant agreement with the experiment measurements, as it could predict the main behaviour of meso/macrosegregation in the solidified ingot. Botton *et al.* [13] suggested that assuming the temperature field to be 2D is a close estimate, because the cavity is confined, the liquid metals are good thermal conductors (fairly low Prandtl number) and the heat flux is in the horizontal longitudinal direction. In contrast, the velocity field cannot be assumed to be close to 2D, because of its changes throughout the transverse direction due to the no-slip condition on the lateral sides. In order to take the three-dimensionality of the velocity field into consideration, an alternative to fully 3D simulations can be obtained by integrating the motion equations in the transverse direction, assuming the specified forms for velocity, temperature and electromagnetic stirring. Note that a reliable representation of the temperature field is one of the major keys to the simulation of solidification problems. We consider that a very first compulsory step towards the implementation of an effective binary alloy solidification model is to validate its ability to: (1) reproduce the temperature field in natural convection configurations; (2) predict the shape and position of the solid-liquid interface in pure metal solidification cases. The uncertainty posed by phase-change problems is the latent heat release at the moving solid/liquid interface, whose position is usually an unknown function of time and space and can determined as a part of the solution. The apparent heat capacity method [14] (AHCM), which has some special computational attributes, is one of the techniques that are applied to process latent heat release for the solidification problems. In the case of forced convection, the application of a magnetic field in the solidification process controls the microstructure and enhances the mechanical alloy characterisations [15-20]. Johnson *et al.* [21, 22] studied the influence of EMS on the microstructure of pure Sn and Sn-Pb alloy. Another aim was to examine in detail the effect of natural convection and forced convection (caused by an induction magnetic field) through the thermally controlled solidification of the pure metal in the pool.

Table 1. Nomenclature

Cp	specific heat, J kg^{-1} K^{-1}	μ	dynamic viscosity, Pa s	g_l	liquid fraction
λ	thermal conductivity, W m^{-1} K^{-1}	$\vec{v}$	intrinsic velocity, m/s	g_s	solid fraction
g	acceleration of gravity, $m.s^{-2}$	p	pressure, Pa	K	permeability, m^2
ρ	density, kg m^{-3}	T	temperature, K	L	latent heat, J kg^{-1}
CR	Cooling rate, K/s	DT	Thermal gradient, K	h	enthalpy, J kg^{-1}
ΔT	melting temperature range, K	D	gaussian distribution	S	porosity
U_T	projected velocity	e	half-width of liquid domain in y direction, mm	Dimensionless number	
A_m	Coefficient of mushy zone				
B	magnetic induction, T	B_0	amplitude of the magnetic field, T	Re	*Reynolds number*
β	thermal expansion coefficient, K^{-1}	F	body force, N	Rm	*Magnetic Reynolds number*
k^*	wave number in narrow liquid domain, m^{-1}	F_x, F_y, F_z	components of the Lorentz force, N	Gr_T	*thermal Grashof number*
				Pr	*Prendtl number*
I A_0	current, A amplitude of the vector potential, T.m	φ	electric potential, V	N_m	non-dimensional interaction parameter
F_0	The magnitude force	σ	electrical conductivity, $\Omega^{-1}m^{-1}$	x, y, z	directions
J_0	current density, $A.m^{-2}$	ω	basic angle frequency, $2\pi f$	Subscripts	
exp, num	*experimental, numerical*	L, H, W	length, height and width of the cavity	l s	*liquid solid*

This paper is based essentially on a comparative experimental and numerical study of solidification problems under the influence of natural convection in which the movement of the fluid is not driven by any external force, but rather by variations in the density of the fluid produced by temperature gradients. Then we examine the case of forced convection generated by Electromagnetic Stirring (EMS) applied in the same direction as natural convection. The effect of both natural convection and EMS on the solidification process was analyzed by using an enthalpy formulation based on a fixed-grid technique solidification model. The numerical results obtained from the full 3D model for natural convection are compared with the experimental results, illustrating the ability of this model to simulate solidification in the presence of natural convection. However, the case of forced convection is only investigated

numerically, and unfortunately not validated against experiment, because there have been no solidification experiments performed on pure tin under electromagnetic stirring carried out with the AFRODITE set-up.

2. Experiment

The benchmark experiment established in the SIMAP / EPM laboratory is a reference tool for the validation of the simulations by comparison with the accurate experimental data obtained with the well-controlled initial and thermal boundary conditions. In its design, the experiment is similar to the well-known Hebditch and Hunt experiment [1], with a particular focus on acquiring reproducible quantitative measurements. A three-dimensional solidification experiment was proposed by Hachani *et al.* [5, 8, 23], with the aim of providing useful quantitative data for the validation of numerical models. The experiment has been performed with pure tin. The experiment consists in solidifying a rectangular sample using two heat exchangers, one on each side, which enable independent control of the sample, horizontal temperature gradient and cooling rate. In the present experimental study, the temperature difference *DT* between the two lateral faces, i.e. left and right exchangers, is 40K and the same cooling rate (CR = -0.03 K/s) is applied in both the right and left walls so that they are cooled simultaneously. This benchmark experiment is a solidification experiment in which the cooling temperature gradient is perpendicular to gravity. Such a setup ensures natural convection and thus macrosegregation in the case of alloys. The choice of the -0.03 $K.s^{-1}$ cooling rate is justified by the fact that macrosegregation and segregated channels can be observed in the solidified ingot at a suitable cooling rate, typically 2-5 $K.min^{-1}$. This slow cooling rate was maintained in order to give sufficient time for thermal convection to become well established in the case of pure materials, and also for rigorous control of the experimental conditions, in particular the heat losses.

To record the instantaneous temperature distribution, fifty thermocouples are welded on the lateral walls. The temperature field time profile is measured and analysed. This helps us to analyse the change caused by natural convection, as well as its effect on the initial conditions of macrostructure solidification. To help understand the results given below, the configuration of the benchmark experiment is shown in Fig. 1. The selected temperature measurements are made on a grid of fifty points numbered from 1 to 50. The heat flux is measured by two groups of thermocouples: FL1 to FL9 and FR1 to FR9 (Fig. 1). The experimental setup consists of five main parts: the sample of pure tin, the stainless-steel crucible with welded thermocouples and the temperature measuring system, the two heat exchangers, the linear motor used to produce a travelling magnetic field, and the Kirchhoff box and the vacuum chamber.

2.1. Measurement procedure

The pure tin pre-sample is enclosed in a rectangular cavity of 100 mm in length, 60 mm in height and 10 mm in width. All walls except for two narrow vertical ones are held in approximately insulating condition during the whole process by means of a Kirchhoff box and

the vacuum chamber. The molten metal is solidified by two controllable heat exchangers. The position of each exchanger is shown in Fig. 1.

Rigorous temperature control is necessary for the two exchange faces and the extracted flux. This is enabled by the high thermal conductivity of copper ($\lambda_{cu} = 380\ W.m^{-1}K^{-1}$) used to make the two exchangers. The choice of copper is deliberate as, although it poses chemical constraints (interaction of copper with tin), it is important thermally. Chemical neutrality is ensured by a thin layer of chromium on the contact face of each exchanger with the liquid metal. Thermocouples FL3 for the left exchanger and FR3 for the right exchanger (closest to the sample-exchanger interface at mid-height) enable control of the temperatures imposed on the exchanger walls, through instructions transmitted to the two thermocouples by a PID (proportional-integral-derivative) automatic controller, which controls the electrical power output of the heating element of each exchanger.

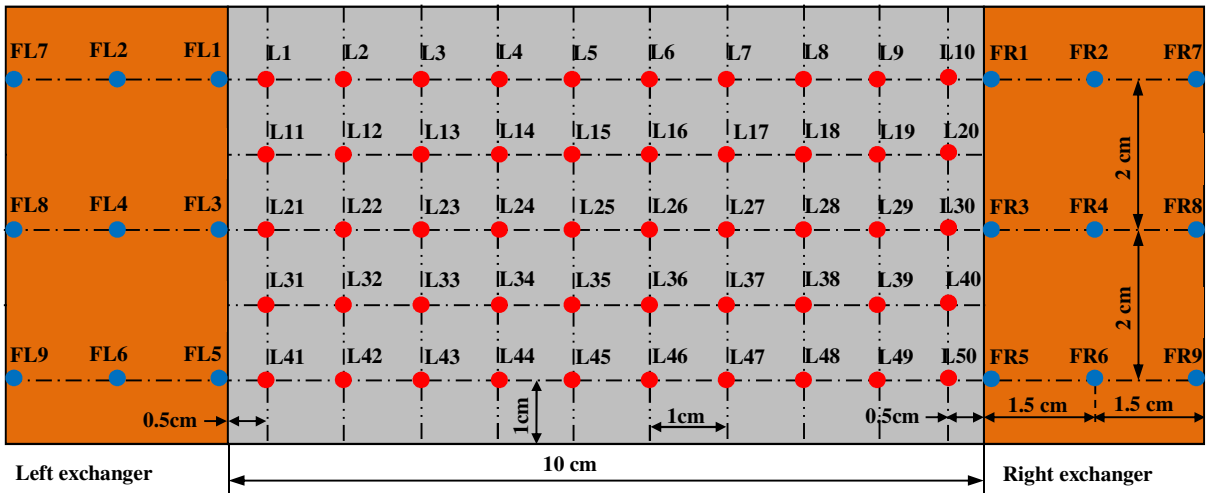

Fig. 1. Diagram illustrating the distribution of all the thermocouples (L1 to L50) welded on one of the larger faces of the crucible, and thermocouples (FL1 to FL9) of the left exchanger and (FR1 to FR9) of the right exchanger.

An array of 50 type K thermocouples placed on the larger surfaces of the stainless-steel crucible records the temperature field every second, tracking solidification progress. The thermocouples have a diameter of 1.5mm, for all the thermal considerations described previously. The fastening of the thermocouples on two side walls of the crucible is the result of a compromise between mechanical resistance, heat losses and easy reproducibility of the fastening process if necessary. All thermocouples are laser spot welded. The welding of all thermocouples is appropriately reinforced to obtain optimum measurement uniformity. It is important to note that all the thermocouples are flush with the load-bearing internal faces of the crucible in order to avoid any effects on the dynamic configuration, in particular the friction with the melt.

The whole experiment comprises five stages shown in Fig. 2: melting, first temperature stabilization to obtain a homogenous temperature field, application of the temperature difference *DT* between the heat exchangers, second stabilization of the temperature field,

sample cooling. The solute was homogenized in the melting phase by electromagnetic stirring, which applies the principle of a linear motor generating an electromagnetic field. This step is very important to control the initial conditions.

Several solidification experiments on pure tin and metallic alloys were carried out. In this work pure tin was chosen in order to validate the numerical approach adopted. The experimental conditions of the present example are: DT = 40 K, cooling rate CR = -0.03 K/s.

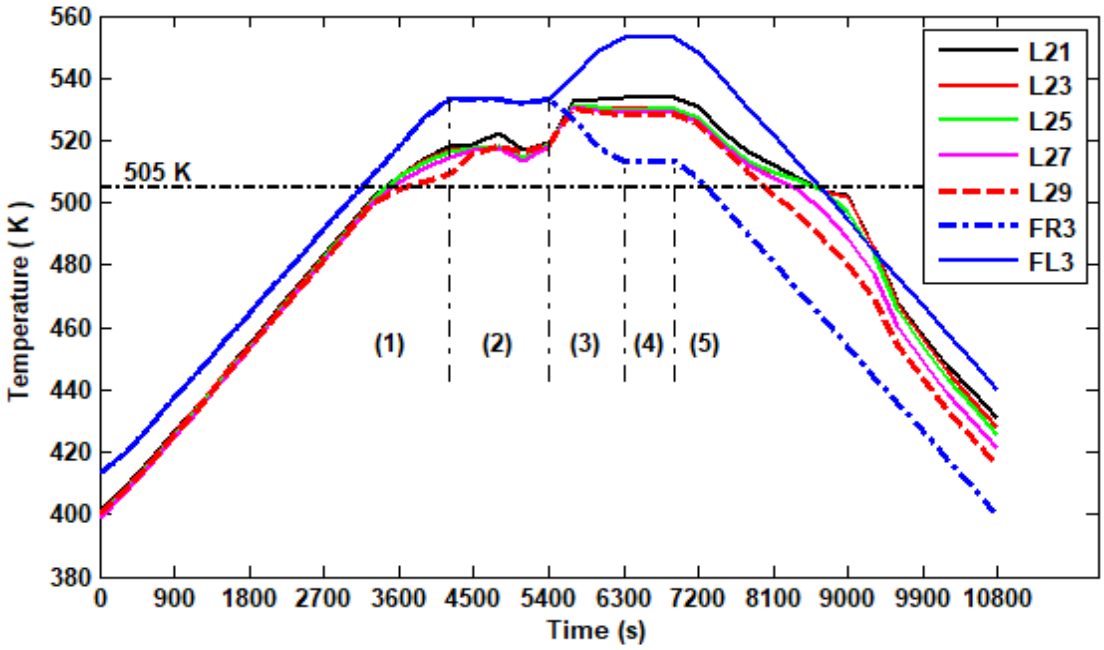

Fig. 2. Time profile of the measured temperature during the solidification of a tin ingot without electromagnetic stirring. The process for all solidification experiments performed consists of five stages: (1) melting, (2) temperature stabilization and electromagnetic stirring to acquire a homogenous temperature field, (3) application of the average thermal gradient, (4) second temperature field stabilization stage and (5) solidification. Applied temperature difference DT = 40 K, cooling rate CR = - 0.03 K/s. FR3, FL3, and L21, L23, L25, L27 and L29 respectively correspond to thermocouples located on the side of the heat exchangers and along the horizontal centreline (mid-height as shown in Fig. 1). The discontinuous black line at 505 K represents the melting temperature.

2.2. Thermal boundary conditions

As discussed in previous work [5, 9 and 10], there may be contact resistance between the two exchangers and the sample. It is significantly dependent on the wettability of the walls by the melt, on liquid motion configurations, and on the distribution and level of the liquid fraction in the sample due to the well-known shrinkage effect during solidification. This means that the actual temperature difference across the bulk of the sample could be small compared with that imposed on the heat exchangers and varies with the transition from liquid to solid state. Furthermore, the cooling rate applied in the lateral sides during the experiment may deviate from the programmed rate if there is intense solidification followed by significant heat release or if the water cooling is inadequate. In order to take these aspects into consideration, the temperature at the inner face of the lateral sample walls is corrected using temperature

measurements obtained by the thermocouples mounted on the heat exchangers and on the front of the cavity near the lateral faces.

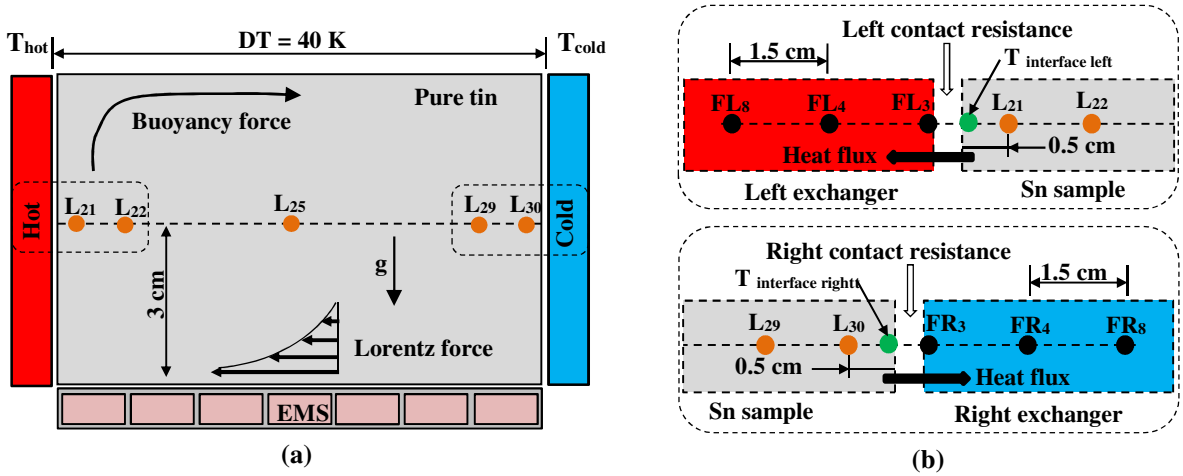

Fig. 3. (a) Diagram of the experimental set-up (AFRODITE) showing the position of some thermocouples: L21 (x = 0.5 cm), L22 (x = 1.5 cm, L25 (x = 4.5 cm), L29 (x = 8.5 cm) and L30 (x = 9.5 cm) all at the same height z = 3 cm and (b) contact resistance between the two heat exchangers (left and right) and the solidifying volume.

In order to estimate the effective temperature difference actually applied to the ingot, it is necessary to extrapolate from the temperatures at the interfaces between the ingot and the two exchangers. These temperatures represent the actual thermal boundary conditions for the numerical simulation. The measurement is based on the concept of conservation of the heat flux exchanged on each side (details of this approach are given in appendix D). Following what is proposed in [8]:

$$\varphi_L = \lambda_{tin} \frac{(T_{left\ interface} - T_{21})}{e} \quad (1)$$

$$\varphi_R = \lambda_{tin} \frac{(T_{30} - T_{right\ interface})}{e} \quad (2)$$

Where λ_{tin} is the thermal conductivity of the ingot, e = 5 mm is the distance between the vertical exchange interfaces and the closest thermocouples (L_{21} and L_{30} for the left and right side respectively). The calculation shows that there are differences between the temperatures measured by the thermocouples FL3 and FR3 (partially in contact with the sample) and the extrapolated temperatures ($T_{Interface\_Left}$, $T_{Interface\_Right}$) of up to about 13 K for the left side and about 7 K for the right side. This can be explained by the existence of significant thermal resistance on each side between the exchanger and the sample.

Note that this resistance needs to be quantified in order to estimate the effective temperature difference applied to the walls of the ingot and to determine the thermal boundary conditions in the numerical simulation models. An extrapolation calculation of the temperature at the exchange interfaces for the case of the solidification of pure tin under an average experimental temperature difference of 40 K and a cooling rate of 0.03 K/s without any

stirring is shown in Fig. 4. The curves of the two extrapolated temperatures show that the effective temperature difference varies around 20 K. An extrapolation method is proposed (finite elements) in order to estimate the heat fluxes exchanged. The development of this approach is explained in Appendix D, including equations (D.7) and (D.8) estimating the heat flows exchanged in the left and right sides.

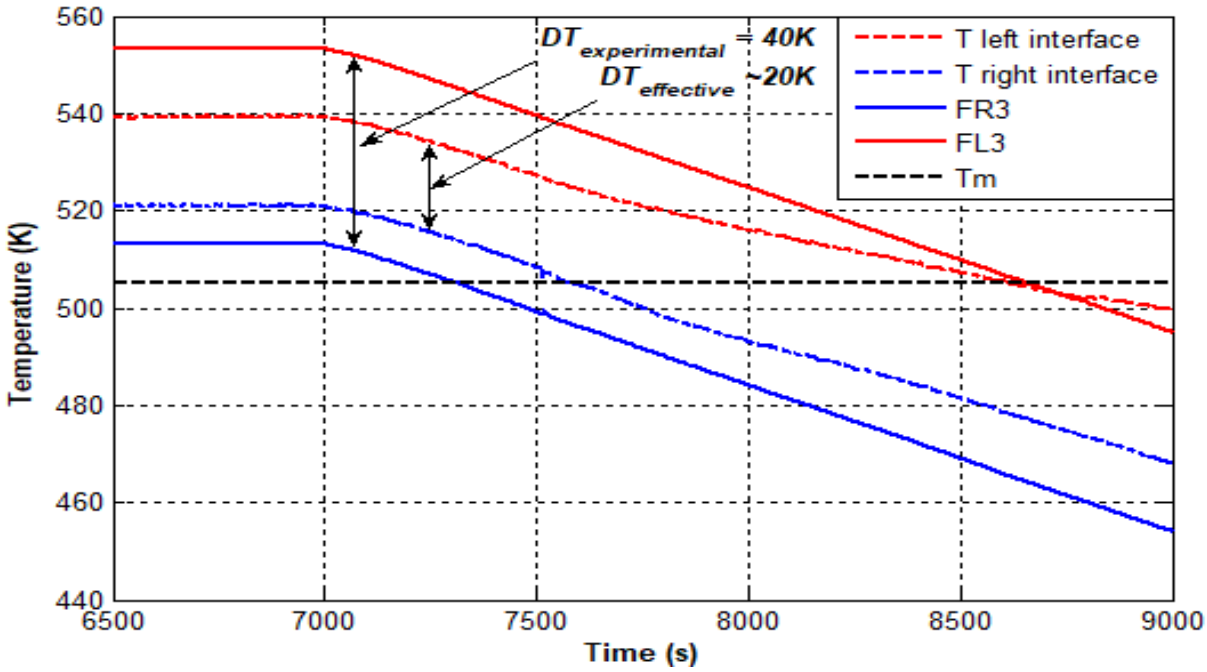

Fig. 4. The experimental time profile of the extrapolated temperatures during the solidification of pure tin. Effective temperature difference $DT \approx 20$ K, cooling rate CR = 0.03 K/s. The time profiles of the right (FR3) and left (FL3) exchangers (see Fig. 1) are also shown. The black discontinuous line represents the melting temperature.

2.3. Control of heat losses

The variation of the heat fluxes measured by the thermocouples located in the heat exchangers with time is shown in Fig. 5. Heat flux conservation is not fully satisfied. However, the relative difference between the left and right heat fluxes is not greater than approximately 12%. Note that the accuracy of the heat flux measurements is limited by the small temperature differences measured in the copper heat exchangers. Despite these issues, the decay of the temperature gradient in the upper-left part of the sample, closer to the end of the solidification, is verified by the low heat flux value given by the thermocouples situated at the top-left of the heat exchanger (i.e. FL1-FL2). This means that the heat flux removed on the wall of the sample is far from uniform.

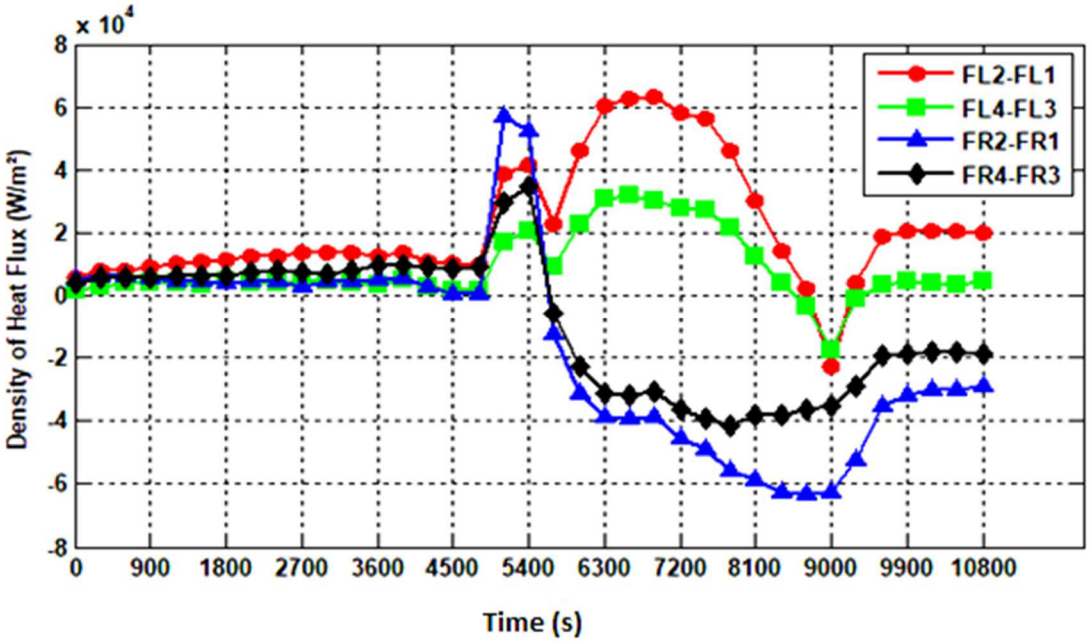

Fig. 5. Time profile of the heat flux density ($-\lambda \nabla T$) obtained from the temperature differences recorded in the two heat exchangers (the thermal conductivity of the copper is 380 $W.m^{-1}.K^{-1}$). The solidification parameters are DT = 40 K, CR = - 0.03 $K.s^{-1}$. FL1, FL2, FL3 and FL4 are the thermocouples placed at the left exchanger, and FR1, FR2, FR3 and FR4 are the thermocouples placed at the right exchanger, as shown in Fig. 1.

Knowing that from the second stage of the experimental process (first thermal stabilization, see Fig. 2), the most dominant heat transfer mode between the crucible and its environment is radiation. In order to compensate this radiation losses and consequently achieve adiabatic boundary conditions on the lateral walls, a temperature controlled Kirchhoff box surrounding the sample was used. It includes a temperature-regulated system comprising the cooling part and the electrical thermal resistance part. An estimate by Stefan-Boltzmann's law of the radiative heat losses through the crucible walls gives an order of less than 1.8 W. Furthermore, heat exchanges by convection and conduction are negligible since the sample is located in a vacuum chamber. In addition, the top surface of the sample was covered with an insulating material, which was sealed in aluminum film to reduce radiant heat transfer.

Special attention is paid to several connections of all thermocouples flushed with the internal lateral faces of the stainless-steel crucible in order to avoid parasitic currents. Indeed, an additional electric current (called the Seebeck current) can be created by any existing parasitic thermal gradient on connections, which relatively distorts the results. In order to avoid this, all connections are contained in a controlled temperature box. The relative accuracy of the temperature measurement is approximately ±0.1 K. However, an offset value could still be present in the temperature measurement. We have corrected this offset by a calibration acquired by pure tin solidification/melting experiments. Since the exact melting temperature of this metal is known, it can be linked to the measured melt temperatures. The remaining uncertainty regarding the absolute value of the temperature is of order of 1 K. All measurements are recorded in ASCII files via a computer.

2.4. Electromagnetic stirring

In the present study, we are mainly interested in analyzing the forced convection effect generated by an external magnetic field (TMF) on the solidification process. The traveling magnetic field is generated by a linear motor placed 5mm under the bottom face of the stainless-steel crucible. Two types of solidification were simulated numerically:

- Case I: The tin melt solidifies only under natural convection. The temperature difference between the two lateral sides of the sample causes a clockwise eddy flow, where the cold wall is situated on the right.
- Case II: The conditions are the same as in Case I, but with application of an electromagnetic force in the same direction as the natural convection. The direction of the flow generated by the electromagnetic force is also in the clockwise direction (see Fig. 3-a). The electromagnetic force is applied during the entire experimental process, i.e. from the beginning of sample melting until the end of solidification, with a working frequency f = 50 Hz.

The main basic equations governing the electrical behaviour of a conductive charge subjected to a magnetic field are the Maxwell equations and the generalized Ohm's law. Within the framework of the magnetohydrodynamic approximation, Maxwell's equations may be found for example in R. Berton [24] and R. Moreau [25]. The body force (Lorentz force) produces stirring inside this fluid. The physical characteristics of the stirring are strongly influenced by the frequency and intensity of the magnetic field used. The expressions of the electromagnetic force were developed by Wang *et al.* [26] for a confined configuration identical to that of our case (F_x, F_y and F_z), and are given in appendix B.

The two components of the active averaged electromagnetic force in the melt can be expressed as follows:

$$\begin{cases} \langle F_x \rangle = \frac{\sigma\omega k^*}{2} A_0 exp(-2k^* z) \\ \langle F_z \rangle = \frac{A_0^2}{2}\left[\sigma\omega\beta^* - \left(\frac{\pi}{2e}\right)\frac{k^*}{\mu}\right] exp(-2k^* z) \end{cases} \quad (3)$$

with $k^{*2} = k^2 + \left(\frac{\pi}{2e}\right)^2$ and $\beta^* = -\frac{\mu\sigma\omega}{2k^*}$.

where σ, ω, k^*, A_0 and e are the electrical conductivity, basic angle frequency, wave number in narrow liquid domain, amplitude of the vector potential and the half-width of liquid domain in y direction, respectively. In this work, the upper index ()* refers to quantities that take into account the narrowness of the fluid domain.

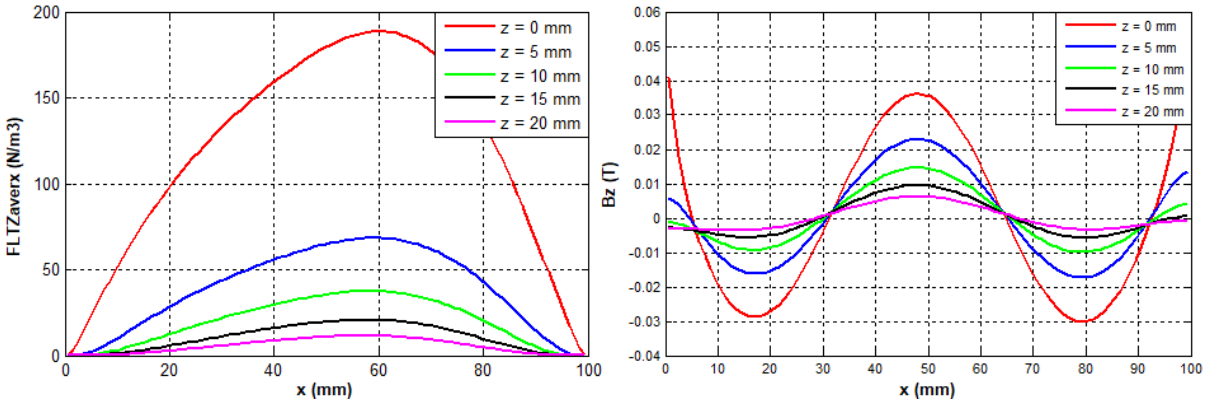

(a) (b)

Fig. 6. Variation of (a) Lorentz force averaged in time in the driving direction (x) and (b) vertical magnetic flux density (B_z) for several vertical levels (z) taken at mid-thickness of the cavity ($y = 5$ *mm*). $f = 50$ *Hz*, $J = 8$ *A* and $A_0 = 2\ 10^{-4}$ *T.m*.

The magnetic Reynolds number is defined as $R_m = uH/\nu_m$, where $\nu_m = 1/\sigma\mu$ is the magnetic diffusivity and u a typical melt velocity. This number, equal to 0.013 in the present experiment, gives an estimate of the relative effects of advection of the magnetic field compared with magnetic diffusion, i.e. the magnetic field will tend to relax towards a purely diffusive state. A numerical simulation of a traveling magnetic field using COMSOL software was carried out under identical geometry and conditions of AFRODITE configuration set-up.

Fig. 6 gives the profile of the Lorentz force contribution in the horizontal direction (x) and the vertical component of the magnetic field (B_z), calculated at mid-thickness of the cavity ($y = 5$ *mm*) for various vertical levels ($z = 0,\ 5,\ 10,\ 15$ and 20 *mm*). Fig. 6 also shows that the corresponding effective skin depth of the magnetic field is approximately $\delta \approx 5$ mm and the corresponding magnetic field amplitude is around *45 mT* for an applied current $I = 8$ *A* and frequency $f = 50$ *Hz*.

3. Numerical model

For simulation of the experiment described above we have used the enthalpy formulation approach, one of the most popular fixed-domain methods for solving phase change problems. The major advantage is that the method does not require explicit treatment of the moving boundary. However, the Stefan problem is based on the assumption that the solid and liquid regions share a moving boundary, which is the phase change front. This corresponds to the multidomain approach previously proposed by Wolf *et al.* [28] and recently used by Avnaim *et al.* [29, 30] to simulate the solidification of pure metals under natural convection. In the multidomain approach the defined domain, corresponding to the chosen geometry, is divided into two regions (one for each phase). The advantage of this method is that the physical properties of the liquid and solid phases are defined separately in each region. It also allows the use of two different mesh refinements.

Enthalpy methods basically account for latent heat in energy equations by allocating a nodal latent heat value to each numerical cell, based on the temperature of the cell. However, the distinction between solid and liquid poses a numerical difficulty, as pure material properties change immediately at the melting temperature T_m. In order to circumvent convergence problems, the enthalpy-porosity formulation implemented in the COMSOL software proposes the introduction of a mushy zone where the thermophysical properties of the solid and liquid phase are spread over a user-defined melting temperature range ΔT (in our study $\Delta T = 1.2$ K). It is well known that the phase transition occurs in a very narrow zone, although the model uses a transition half-width, ΔT. It would be even more evident if pure metal were cast, but somewhat wider if the cast materials were an alloy with a larger ΔT. If we want to reduce ΔT further to model the casting of some pure metal (as in our case: ΔT = 1.2 K for pure tin), we would need to increase the mesh resolution and consequently the simulation becomes very costly in terms of computing time, more particularly for a 3D geometry.

From the numerical simulation point of view, the choice of the temperature transition range ΔT requires careful consideration. The sharp gradients of the modified heat capacity may lead to convergence issues if ΔT is small (e.g. ≈ 0.1 K) and the mesh resolution at the interface does not cover the imposed range. A small ΔT means higher accuracy but with greater computational effort. A qualitative initial choice in the range of 5 K may be used (Murray and Groulx, [27]). A reasonable trade-off between precision and computational effort is obtained in the test cases of the present analysis with the chosen value of 1.2 K. The work is carried out with the commercially-available COMSOL Multiphysics™ software, which offers a suitable user-input environment for implementing the enthalpy-porosity method.

The principal advantage of the porosity formulation is the use of only a single mesh to solve the equations governing fluid flow and heat transfer. However, stable coupling to CFD for buoyant and Lorentz forces requires additional user treatment by defining the set of complimentary algebraic equations for material proprieties. Latent heat during a phase change is incorporated in the energy equation using the following definition of enthalpy for each phase:

$$h = CpT + \Delta H \tag{4}$$

where $\Delta H = g_l(T).L$, L is the latent heat, C_P the specific heat coefficient and $g_l(T)$ the liquid fraction defined by Eq. 5 and shown in Fig. 7(a):

$$g_l(T)\begin{cases} 1 \; for \; T > T_m + {}^{\Delta T}/_{2} \\ \frac{T-(T_m-{}^{\Delta T}/_{2})}{\Delta T} \quad for \;\; T_m + {}^{\Delta T}/_{2} \geq T \geq T_m - {}^{\Delta T}/_{2} \\ 0 \; for \; T < T_m - {}^{\Delta T}/_{2} \end{cases} \tag{5}$$

The specific heat is expressed as a function of the latent heat L (see Fig 7(b)) and the Gaussian distribution function $D(T)$ as follows:

$$Cp(T) = Cp_s + g_l(T).(Cp_l - Cp_s) + D(T).L \tag{6}$$

With:

$$D(T) = \frac{e^{-\left(\frac{T-T_m}{\Delta T/4}\right)^2}}{\sqrt{\pi}\Delta T/4} \qquad \text{(see Fig. 7(c))} \tag{7}$$

During solidification, latent energy is released at the interfaces that separate the liquid and solid phases. Thus, the energy equation can be written as, [31]:

$$\frac{\partial \rho h}{\partial t} + \nabla(\rho u h) = \nabla(\lambda \nabla T) \tag{8}$$

By using Eq. 4 and $\Delta H = g_l\,(T).L$, the energy equation will be defined as follow:

$$\frac{\partial(\rho C_p T)}{\partial t} + \frac{\partial(\rho g_l L)}{\partial t} = -\nabla(\rho u h) + \nabla(\lambda \nabla T) \tag{9}$$

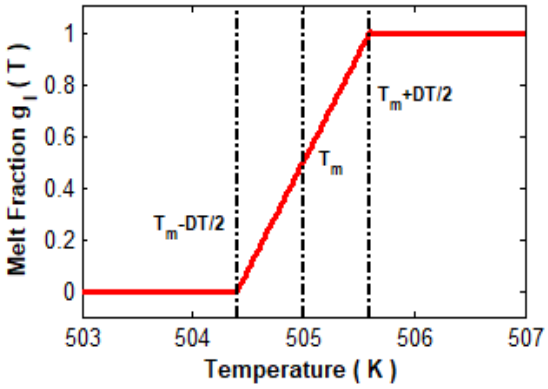

(a) Melt fraction function $g_l(T)$, implemented as a piecewise function

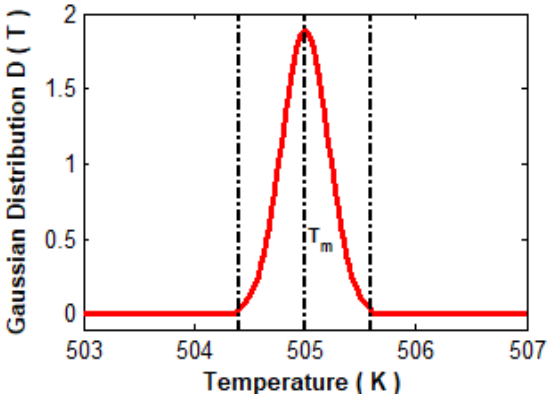

(b) Gaussian distribution function $D(T)$, for $\Delta T = 1.2$ K.

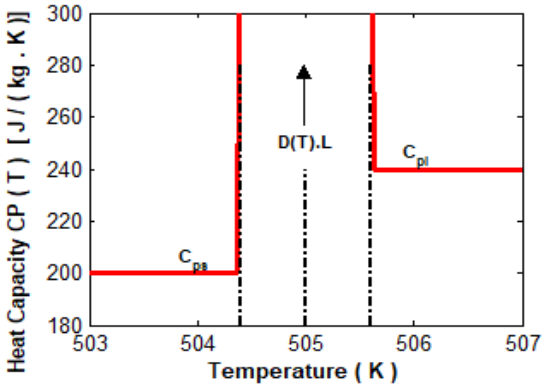

(c) Heat capacity function Cp(T), rising to a the maximum value of D(T).L = 120000 J.kg^{-1}.K^{-1}.

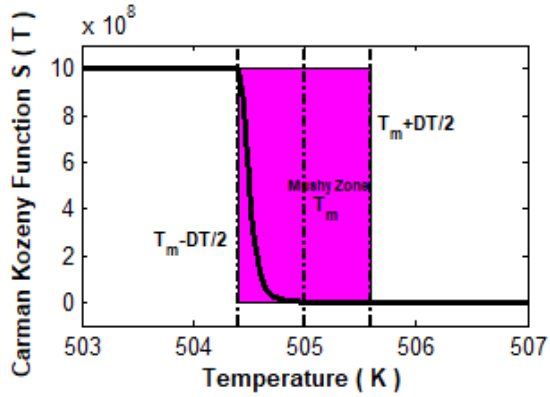

(d) Carman-Kozeny function to model sink-term and viscosity of the solid fraction.

Fig. 7. Temperature-dependent modelling functions implemented in the numerical model for pure tin.

where ρ is the density, λ is the thermal conductivity and u is the flow velocity, and the unsteady latent heat L content term on the left side of Eq. 9 is equal to zero for $T < T_m$-$\Delta T/2$ and $T > T_m$+$\Delta T/2$ (it influences the energy equation only within a user defined temperature range ΔT).

An important basic assumption with fixed-grid solution techniques is that establishment of a zero-velocity condition is required in cells when a liquid area becomes solid. Numerous methods may be used, in principle, to "switch off" velocities in computing cells that are freezing (or "turn on" velocities in the case of melting). The momentum equation part of the study requires an additional modelling term $S(T).u$ in the governing equations (Eq. 10), accounting for the porosity of the mushy zone. The porosity function *S(T)* is derived from the Carman-Kozeny equation (Eq. 11).

The incompressible momentum equation assumes constant density yielding:

$$\rho\frac{\partial u}{\partial t}+\rho(u.\nabla)u=\nabla(\mu(T).\nabla u)-\nabla p-S(T).u+F \tag{10}$$

$$S(T)=A_m\frac{(1-g_l(T))^2}{g_l(T)^3+\epsilon} \tag{11}$$

with:

$$F=\underbrace{\rho g\beta\Delta T}_{Buoyancy\ force}+\underbrace{(J\times B)}_{Lorentz\ force} \tag{12}$$

with the modelling constants A_m = 10^6 kg.m^{-3}.s^{-1} and ϵ = 10^{-3} (Samara *et al.*, [32]; Kheirabadi and Groulx, [33]). The function *S(T)* is a sink-term in the momentum equation. In the case of a solid fraction, the momentum equation (Eq. 10) provides a trivial (u = 0) solution to ensure immobility. As illustrated in Fig. 7(d), the *S(T)* impacts both the solid fraction and the solid-dominated part of the mushy zone ($T < T_m$). The simulating term *S(T)* overrides any other term in the momentum equation in the solid zone. However, it is proposed that the viscosity [33] in COMSOL Multiphysics™ be further updated in order to achieve convergence in the model as follows:

$$\mu(T)=\mu_l\big(1+S(T)\big) \tag{13}$$

with the empirical viscosity-temperature relation (E. V. Rozhitsina *et al.*, [34]), for pure tin,

$$\mu(T)=31\times10^{-5}\left(\frac{6.171\times10^3}{RT}\right) \tag{14}$$

where T is given in [K] and the dynamic viscosity μ_l in [Pa s]. Consequently, the dissipation term in the momentum equation overrides the other terms within the solid regime. This method guarantees that flow is induced only in the liquid fraction within the computational domain despite the solving of the momentum equation for both solid and liquid fractions.

The conservative form reads for a pure substance (e.g. pure tin):

$$\nabla(\rho u)=0 \tag{15}$$

The A_{mush} is an important factor for specifically modelling phase change heat transfer in particular, high A_{mush} values coinciding with slow solidifying rates and low A_{mush} values resulting in unphysical predictions of the solidification front. In addition, it was found that A_{mush} and ΔT are not independent of each other directly in their functions modelling the

solidifying rate. One value of ΔT would require different values of A_{mush} to obtain a satisfactory solidification front showing good consistency with the experimental results. A reasonable compromise obtained from several tests, avoiding the slower solidifying rates and also the unphysical predictions of the solidification front in this study for a temperature transition range ΔT equal to 1.2 K, is $A_{mush} = 10^6$ kg.m^{-3}.s^{-1}.

4. Results and discussions

Three-dimensional simulations are performed with the grid comprising 242125 elements and their results are presented in this section, obtained with $J = 8$ A and magnetic vector potential $A_0 = 2\ 10^{-4}$ T.m in the expression for the electromagnetic force (Eq. 3). The Delaunay tetrahedralization mesh generator is used. The time stepping method used in the implicit time-dependent solver is a free backward differentiation formula (free BDF). A segregated solver is used, where a Newton method is still applied at each time step, but for the different variables separately and with minimal Jacobian update and the Newton corrections are obtained by an iterative solver (GMRES) for the velocities and pressure and by a direct solver (PARDISO) for the temperature. As well known in the case of solidification simulation, prospective strong nonlinearity can arise as a consequence of physical domain properties being a function of the solution, or to feedback of solved equations. Indeed, to avoid this problem, the implicit time dependent BDF solver (free backward differentiation formula) chosen in our numerical model is computing the solution to a possibly nonlinear system of equations at each time-step via a set of iterative techniques based upon Newton's method. If these iterative techniques fail at any time-step, the predefined algorithms in the free-BDF solver increment the resolution column called NLFAIL. These Newton's method techniques for solving a nonlinear system of equations evaluate a function, as well as its derivative, at every time-step. This derivative is also known as the Jacobian and is relatively expensive to compute. Therefore, the COMSOL software will try to minimize reevaluating the Jacobian, by default. If the nonlinear solver has difficulty converging, it will reduce the requested time-step size and try to compute the solution. When the time-step is reduced, another column (TFAIL) is incremented. This is a suitable approach if the solution fields vary rapidly in time, as the case of phase change problems. In addition, numerous mesh refinements were used to examine the convergence of the model implemented and the minimal refinement to ensure the mesh independence of the given solution was used. Physical properties of the pure tin are given in the Table B.1 (in Appendix B).

The initial step in numerical simulations corresponds to the uniform distribution of the temperature gradient inside the cavity corresponding to the temperatures 541.29 K and 521.24 K applied at the left and the right lateral sides, respectively. This corresponds approximately to 16900 s of the physical time in the solidification experiment shown above in Fig. 4. Multiple physical phenomena are strongly coupled in this multidisciplinary process. The configuration of fluid flow which is governed by electromagnetic and buoyancy forces significantly affected the temperature distributions and consequently the phase transition. Furthermore, solidification is accompanied by heat release that also affects the temperature field. The evolution of the temperature distribution was measured every second during the experiment, which could serve as principal reference for validation between numerical results

and those obtained experimentally. Therefore, analysis of the results begins with presentation of the effect of electromagnetic stirring on the dynamic behaviour before solidification i.e. during the second thermal stabilization stage (stage 4), and then the evolution of the temperature field during solidification. The analysis continues with description of the solidification process with evolution of multiphase flow and phase fraction.

4.1. Effect of electromagnetic stirring on dynamic configuration

The ability of the 3D model to predict the velocity and temperature fields before solidification (stage 4 in Fig. 2) within the cavity is shown in Fig. 8. The velocity fields are represented as coloured magnitude levels and black vectors, while the temperature fields are represented by black isotherm lines.

The purpose of this study is to verify the effect of the EMS on the velocity and thermal behaviour by comparing natural and forced convection (with and without EMS).

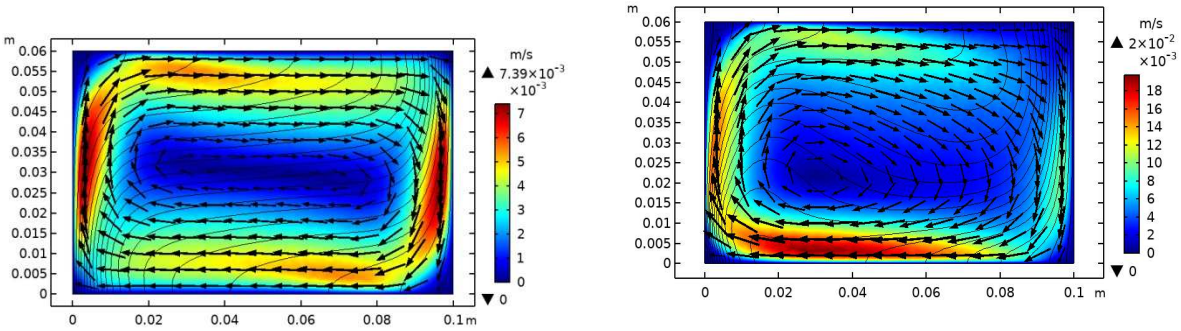

(a) ***(b)***

Fig. 8. Velocity fields (coloured magnitude levels and arrows) and temperature field (isotherms) obtained without solidification and with different convection: (a) 3D model for natural convection (view in the vertical middle plane), (b) 3D model for forced convection (electromagnetic stirring in the same direction as natural convection).

The results obtained for the case of natural convection are reported in Fig. 8(a) in a cross-section plane (*xz*) located at mid-thickness in the transverse direction *(y =5 mm)* over the small width *W*, while Fig. 8(b) shows results obtained with forced convection. One vortex appears in each case, the first (case (a)) located at the centre of the cavity and the second (case (b)) located in the middle-left part of the sample near the hot wall, with a highly convective flow. It can clearly be seen that the isotherms are more deformed in case (b) than in case (a), especially in the region where the velocity is maximum at the level of the magnetic skin. There is also a marked increase (about 10-fold) in the velocity value due to the application of EMS, which can generate large motions in the liquid bath. This comparison confirms that the application of EMS has a direct effect on the velocity field and thermal behaviour in the liquid bath in term of the velocity value and the shape of the isotherms.

It is important to introduce the thermal Grashof number based on the vertical aspect ratio, (*H/L*), which is set at (3/5) in the present work as follows:

$$Gr_T = \frac{g\beta_T \Delta T\left(\frac{H^4}{L}\right)}{\nu^2} \quad (16)$$

where ν is the kinematic viscosity (ν = 2.54 10^{-7} m².s^{-1}).

Before the solidification stage, parameter Gr_T (8.67×10^6) is the most relevant parameter for describing natural convection. It is also important to compare electromagnetic forces with buoyancy using a dimensionless interaction parameter N_m, expressed as the ratio of Lorentz forces to buoyancy:

$$N_m = \frac{F_0}{g\rho\beta_{T\Delta T}} \quad (17)$$

With F_0 the force obtained from (Eq. 3):

$$F_0 = C\frac{\sigma\omega k^* B_0^2}{2} \quad (18)$$

Where $C \approx 0.05$ is a coefficient that takes into account the finite size of the inductor [25].

In the present study, the value of N_m is 4 for B_0 = 45 mT (or J = 8 A). Electromagnetic forces are thus dominant compared with buoyancy. Lastly, before solidification, the Reynolds number based on the average velocity (u_{aver} = 0.01 m/s) is:

$$Re = \frac{u(u=1)\left(\frac{H^2}{L}\right)}{\nu} = 1440 \quad (19)$$

The value of Re indicates that the bulk flow regime is likely to be laminar for the case of rectangular cuboid geometry.

4.2. Comparison of projected velocity between experiment and numerical simulation

This paragraph is devoted to the comparison between the velocity field obtained in the simulations for pure thermal convection, i.e. during stage 4, and a particular approach in experimental analysis: projected velocity. The experimental data from the temperature field are analysed to obtain some clues about the dynamic configuration during the solidification process, including the magnitude of the velocity field in the liquid zone. The method consists in calculating the magnitude of the projected velocity U_T on the temperature gradient vector at each node corresponding to the position of a thermocouple. Such an approach is valid as long as the Peclet number is high, meaning that convection is significant. L. Hachani *et al* [8] provide further details concerning this approach.

The principle of the method [23], is based essentially on integrating the heat equation over the thickness of the sample in the liquid region as follow:

$$\int_0^e \frac{\partial T}{\partial t} dz + \int_0^e \vec{U}.\vec{\nabla}T\, dz = \alpha \int_0^e \nabla^2 T\, dz \quad (20)$$

where $\vec{U}$, α and e are the instantaneous velocity field, the liquid thermal diffusivity and the thickness of the sample, respectively. If we assume that the temperature field is uniform in the

transverse direction, which is confirmed experimentally, then the integral of Eq. 20 is reduced to:

$$\frac{\partial T}{\partial t} + \vec{u}.\vec{\nabla}T = \alpha\nabla^2 T \quad \text{with } \vec{u} = \frac{1}{e}\int_0^e \vec{U}\, dz \tag{21}$$

The estimated algebraic velocity U_T is defined as follows:

$$U_T = \vec{u}.\vec{\nabla}T/\left|\vec{\nabla}T\right| \tag{22}$$

The vector $\vec{u}$ is the average value of the instantaneous velocity across the thickness of the sample, where $\left|\vec{\nabla}T\right|$ is the norm of the temperature gradient.

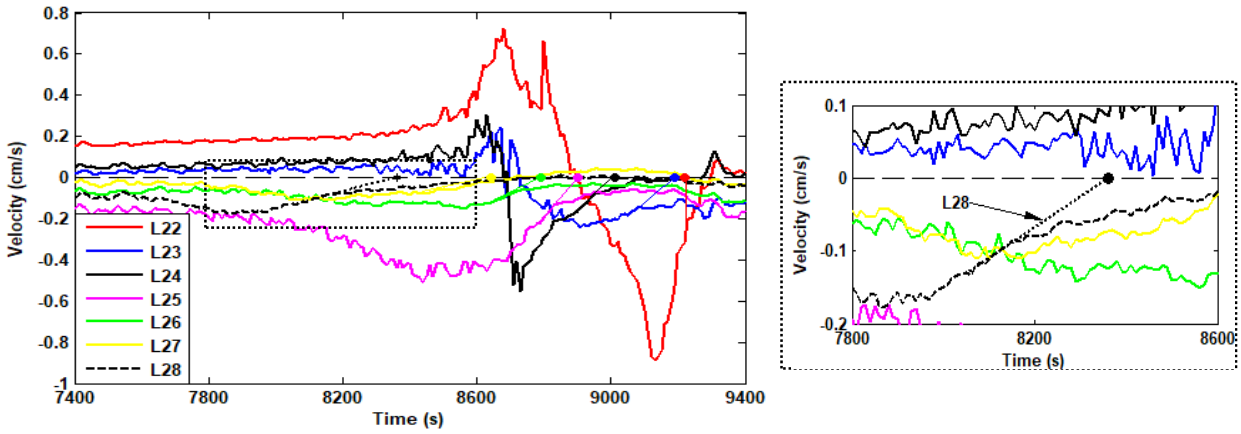

Fig. 9. (a) Time profile of the modulus of the projected velocity *U* for different internal nodes (L22, L23, L24, L25, L26, L27, and L28) located at mid-height of the ingot. Fig. 8 also shows the extrapolation to zero used to estimate the time when the solidification front passes through the position of the nodes. Pure Sn, *DT* = 40 K, CR = 0.03 K/s. (b) zoomed-in view of projected velocity at the node corresponding to thermocouple L28.

In order to obtain the value of U_T, we have discretized the heat equation in the liquid state (without latent heat release) using the finite difference method. Details of this method are given in appendix A. We then obtained and introduced the measured temperature data, and the results are shown in Fig. 9.

Fig. 9 shows the time profile of the projected velocity on the thermal gradient vector at nodes L22, L23, L24, L25, L26, L27 and L28 (see Fig. 1) located at mid-height in the ingot, where the scalar products of the velocity vector $\vec{u}$ and the temperature gradient $\vec{\nabla}T$ are assumed to be not too small. The velocity decreases as the solidification front reaches the node. The velocity is observed to increase during solidification (for example, node L25 in Fig. 9(a)), then decreases almost to zero (node L28 in Fig. 9(b)). We have calculated the time when the velocity decreases to a value near to zero by extrapolating the velocity curve to zero using the tangent measured at the inflection point (see Fig. 9(b)). The use of this technique was justified by the fact that the approach described earlier in this paragraph is no longer accurate when the node coincides with the solidification front, because the latent heat release has not been taken into account.

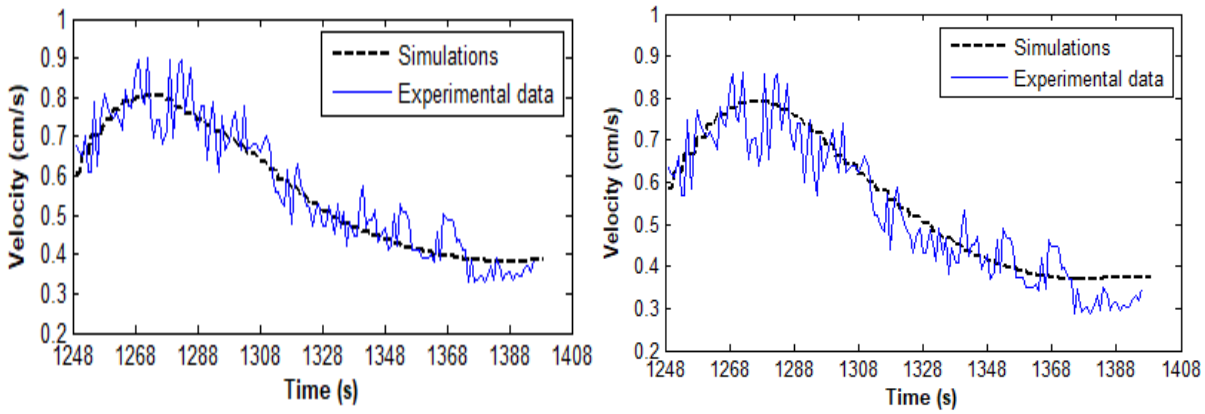

(a) (b)

Fig. 10. The time profile of the projected velocity on thermal gradient [8] between the 3D model (black discontinuous line) and the experiment (blue continuous line) for nodes L22 (a) and L23 (b).

In Fig. 10 the projected velocity U_T for nodes L22 and L23 obtained from the experimental data (continuous line) and 3D numerical simulation (discontinuous line) are shown for a period of 160 seconds during the pure convection period (before solidification and without any stirring). It can clearly be seen that the projected velocity profiles obtained by simulation and by experimental measurement are in good agreement. Furthermore, the projected value of U_T at node L22 is higher than at node L23, where the velocity is almost perpendicular and the velocity at the sides is higher than in the centre.

4.3.Temperature evolution: experiment/numerical simulations

The instantaneous temperature maps in Fig. 11 show the thermal changes during the solidification process (stage 5 in Fig. 2). The maps of pure thermal convection (case I) and forced convection with EM stirring (case II) are compared with the experimental results (Exp in Fig. 11). The temperature field is recorded in the vertical middle plane at the same level as the thermocouples. However, it is shown that the temperature field illustrated as 2D gives a clear representation of the main circulation side. It is important to note that the experimental results are obtained within the zone covered by the array of 50 thermocouples shown in the central column in Fig. 11 for the experimental results. This zone is marked by the white rectangle on the numerical results for both cases simulated, i.e. natural convection (left column) and forced convection (right column). The time profile of the solidification process is illustrated in Fig. 12, showing a good agreement between the numerical and experimental results (case I and Exp).

At t = 7609 s the sample is completely liquid. The behaviour of both numerical cases and experimental temperature fields shows that, despite the low value of the Prandtl number ($Pr \approx 0.015$), the isotherms are strongly deformed by convection, especially in the case of forced convection. The convection, generated by the application of a horizontal temperature gradient in case I and by electromagnetic stirring in case II, takes the form of a single vortex, which occupies almost the whole cavity and goes up the hot wall and down the cold wall. The

maximum velocities obtained by simulation at this stage are 0.739 cm/s and 2 cm/s for natural and forced convection, respectively (Fig. 11(a)).

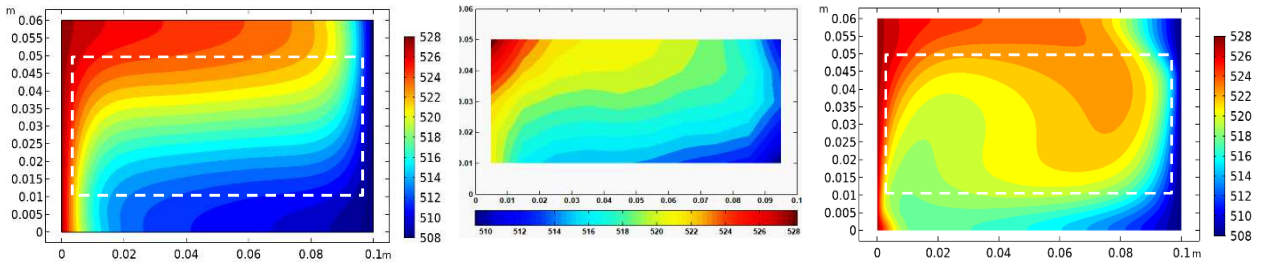

Case I **Exp** **Case II**

(a) t = 7609 s

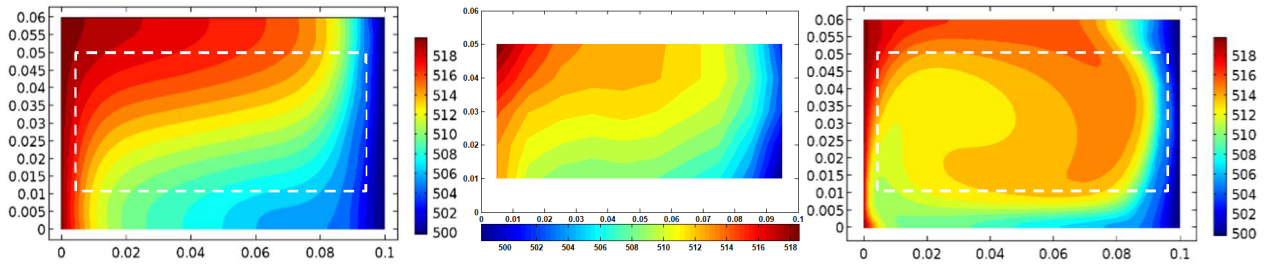

Case I **Exp** **Case II**

(b) t = 7897 s

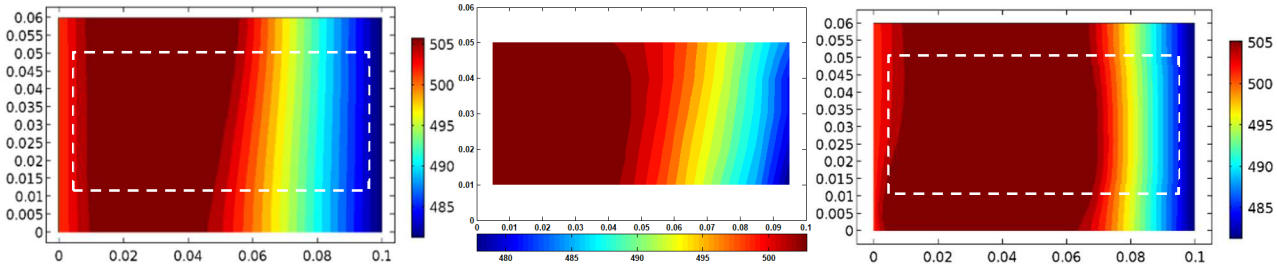

Case I **Exp** **Case II**

(c) t = 8735 s

Fig. 11. Temperature maps at selected instants during the solidification of a pure tin: (a) t = 7609 s, (b) t = 7897 s and (c) t = 8735 s. Case I, Exp and Case II correspond to the numerical calculations for the case of natural convection (on the left), the experimental data (in the centre), and the numerical calculations for the case of forced convection (on the right), respectively. The white dashed rectangle on the numerical snapshots represents the part of the domain in which thermocouples are present. Conversely, the white stripe all around the colour map in the experimental snapshots corresponds to the part of the domain in which no thermocouple is present. The temperature colour bar scales are in Kelvins.

At t = 7897 s (Fig. 11(b)), the sample is still mainly liquid. However, the first solid crystals appear on the colder side (right end of the sample) because the cold temperature is now below the melting temperature. The isotherms in the right part of the sample, which is now solidified, gradually become vertical with mainly conductive transfer and progressively move

towards the left side as the temperature decreases. It can also be noted that the flow is still strong enough to deform the isotherms. In contrast, the isotherms in the case of forced convection are more deformed than in the case of natural convection. This behaviour is due to the higher velocities generated by the electromagnetic force.

At t = 8735 s, a second solidification front has appeared on the left side of the sample, because the temperature imposed on this side (the hotter side) is now below the melting temperature of pure tin (505 K). The solidification front has progressed from the right to the left compared with the previous snapshots. The isotherms in the liquid zone are also less deformed than the first snapshots. However, the thermal gradient is low in the liquid bath, as shown by the increased space between successive isotherms at t = 8735 s. The liquid phase located between the two fronts is progressively disappearing to give an overall solid zone. The left and right solidification fronts will meet at 8770s (Fig. 11(c)).

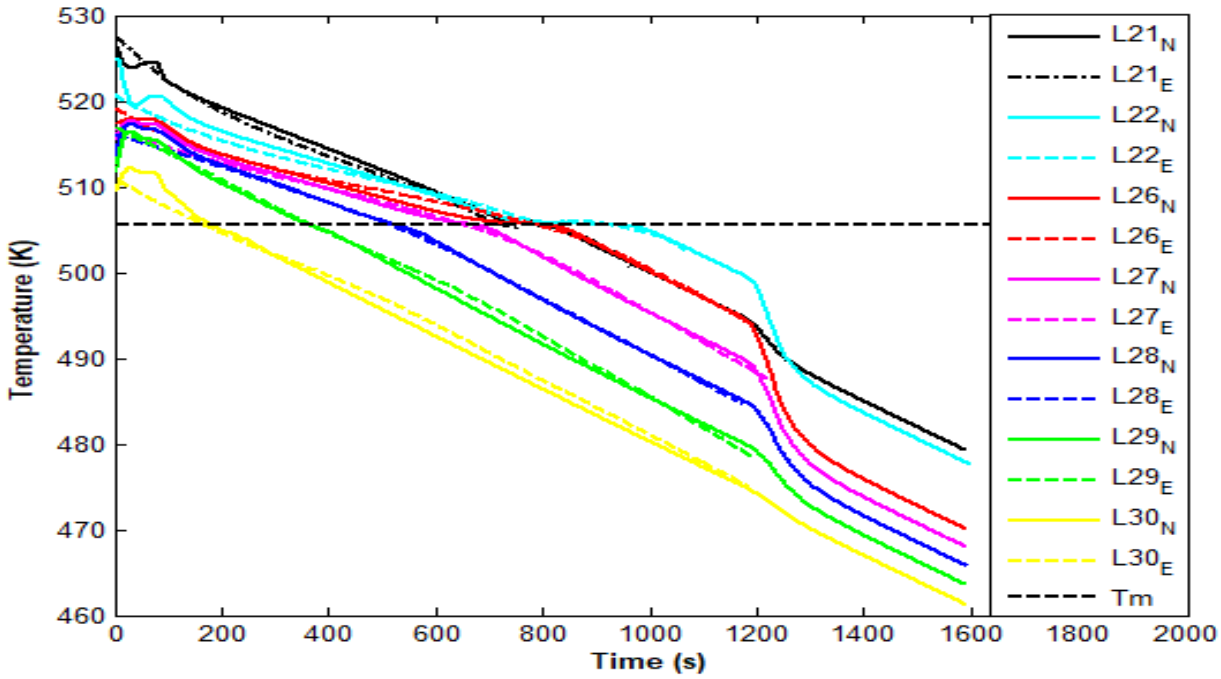

Fig. 12. Numerical (subscript N) and experimental (subscript E) time profiles of the temperature at some thermocouple positions (see Fig. 1) during the solidification process (without any stirring). The melting temperature T_m is represented by the dotted line.

The temperatures of all the thermocouples decrease slowly until they reach the melting temperature. They stabilize at the phase-change plateau, then continue to decrease. The thermocouple L_{30} (yellow line) near the colder wall is the first temperature signal to decrease below T_m. The temperature of the latter will leave the plateau value at T_m, indicating the front appearing on the right side, which then advances to the left. The second solidification front appears on the left side when L_{21} (thermocouple closest to the hot wall) decreases below T_m. In addition, it can be seen that the thermocouples L_{21} and L_{26} (the black and the red lines, respectively) leave the phase-change plateau of pure tin at the same time. This means that the solidification front which advances from the right (the first front) arrives at L_{26} at the same time as the second front arrives at L_{21}.

4.4. Deviation between temperature fields

Fig. 13 shows the temperature deviation between simulation and experimental measurements during the solidification stage without any external force applied (natural convection only) measured by the thermocouples in middle line of the sample (L21, L22, ... L30). We define the following estimators of the difference between the experimental and the numerical solutions in the vertical middle plane:

$$\Delta \max_i \left| Temp\_exp_i - Temp\_num_i \right|_{max} \quad (23)$$

where *Temp_exp* and *Temp_num* are the experimental and the numerical temperatures in the case of natural convection.

Using the temperatures at the 50 thermocouple positions, we can also define the relative deviation $\Delta_{num/exp}$ between the numerical prediction and the experimental measurements:

$$\Delta \frac{1}{50} \sum_{i=1}^{50} \left| \frac{Temp\_exp_i - Temp\_num_i}{\Delta T} \right|_{num/exp} \quad (24)$$

Fig. 13 presents three different snapshots of the spatial evolution and normalized deviation of the temperature field during the solidification process, for the given Grashof and Prandtl numbers. The maximum relative deviation was estimated by the temperature profiles of numerical simulation and experimental measurements in the horizontal middle line of the cavity represented by the thermocouples L21 to L30 (see Fig. 1). Normalized deviation of the temperature field in the middle plane at different times was also estimated for Gr = 8.67×10^6 and Pr = 0.0015.

Fig. 13(b) also gives a typical map of the deviation, obtained for Gr = 8.67×10^6 and Pr = 0.0015. It can be seen that the region of high deviation corresponds to the zones where the flow exhibits separation from the wall and recirculation in the centre. This shows that the effectiveness of this type of model is linked with its ability to predict the convection heat transfer and heat losses in the corners of the cavity. The relative deviations are 4.82%, 4.59%, 3.66% and the maximum deviations Δ_{max} are 2.16, 2.31, 2.99 at t = 7609 s, t = 7897 s and t = 8735 s, respectively. The comparison between the experimental and numerical results on the longitudinal temperature profile along x_1 at mid-height is plotted in Fig. 13 (a) and (b). It can be seen that the 3D numerical profile is very close to the experimental values of the temperature, with deviation principally at the left and right boundaries of the sample (thermocouples L21, L22 and L29, L30). This behaviour is due to the shrinkage that occurs at the cold and hot sides.

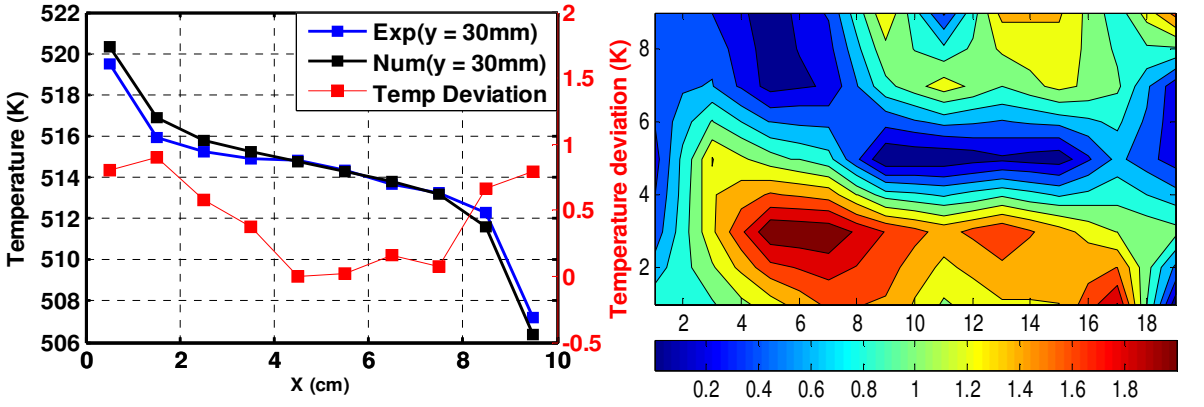

(a) *t = 7609 s* *(b)*

$\Delta_{num/exp} = 4.82\%$, $\Delta_{max} = 2.16$

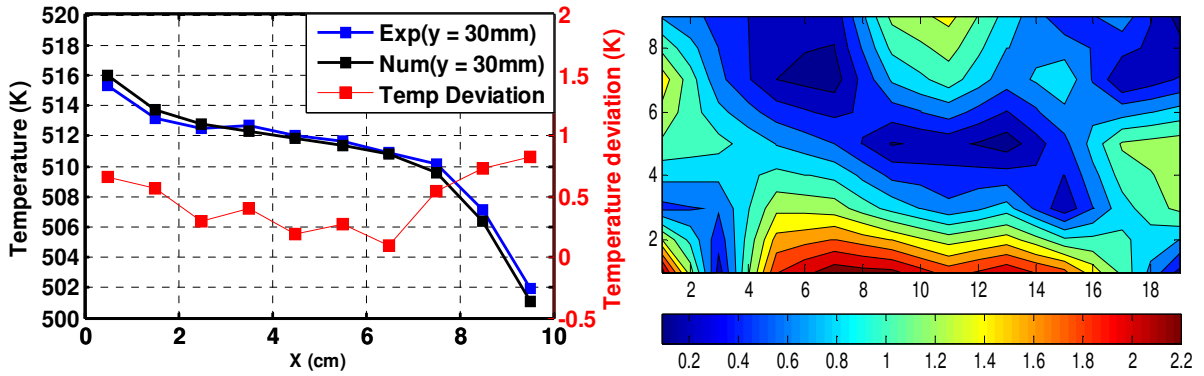

(a) *t = 7897 s* *(b)*

$\Delta_{num/exp} = 4.59\%$, $\Delta_{max} = 2.31$

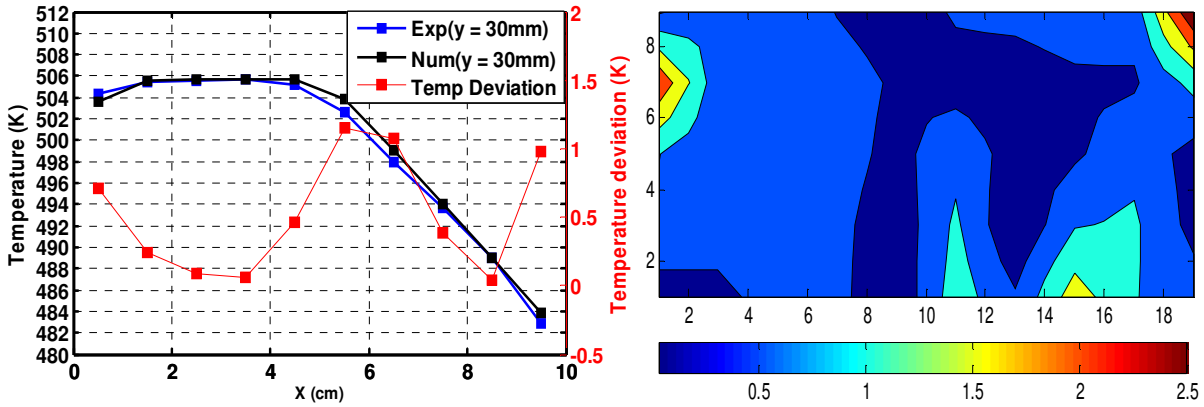

(a) *t = 8735 s* *(b)*

$\Delta_{num/exp} = 3.66\%$, $\Delta_{max} = 2.99$

Fig. 13. (a) Numerical (black) and experimental (blue) spatial evolution of the temperature field along the line defined by thermocouples L21, L22, ... L30. (b) corresponding deviation maps.

4.5. Comparison of the solidification front evolution between experiment and numerical simulations

In the light of the previous comparisons between the three cases in terms of temperature behaviour, we have shown the need to study the effects related to the morphology of the solidification front with the same initial boundary conditions as defined in the previous part. Solidification starts when the first solid crystal is formed in the liquid bath and continues until there is no trace of any liquid in the system (see Fig. 11). In Fig. 14 below, three different instantaneous colour maps of the progress of the solidification process over time show an exposition between the two numerical simulations and the experimental results during the process.

At t = 7840 s, T_C is the first temperature in the sample to go under T_m. The solidification starts from the right side where the sample is mainly liquid. A tilted vertical solid front appears on this side under the effect of the thermal gradient. Electromagnetic stirring also has a strong effect on the shape of the solidification front, as illustrated in Fig. 14 (b) and (c) case II.

At t = 8450 s and t = 8510 s, the three cases clearly show the progress of the solidification front from right to left. The shape of solidification front is fairly similar in the experimental measurements and the numerical simulation for natural convection (Exp and Case I in Fig. 14). The inclination of the solidification front is caused by the thermal gradient. At about 8450 s, the solidification front moves back towards the sidewall, indicating that remelting has occurred. The phase change releases a certain amount of latent heat from the melt, and there is not enough time for it to be extracted by the heat exchangers. It is important to note that the curvature of the solidification front is relatively accentuated and its advance is delayed in case II due to the effect of electromagnetic stirring compared with that of natural convection. The solidification resumes its progress as the latent heat is extracted. Natural convection becomes weak, and the liquid volume decreases. In contrast, a second solidification front appears later during the process on the left side of the cavity (see Fig. 14 (b) and (c)), when the hot temperature of the left heat exchanger drops below T_m.

Lastly, at t = 8680 s, both fronts progress, reducing the liquid region. The last liquid in the cases of natural convection simulation (case I) and experiment (Exp) is located in the upper-middle portion of the sample. In contrast, in the case of forced convection, the last liquid is located in the left bottom-middle portion of the sample (case II in Fig. 14(d)) due to the higher velocity generated by the electromagnetic force. The application of electromagnetic stirring also prevents the germination of solid crystals. The latent heat release plays a predominant role, more significant than natural convection, during this period.

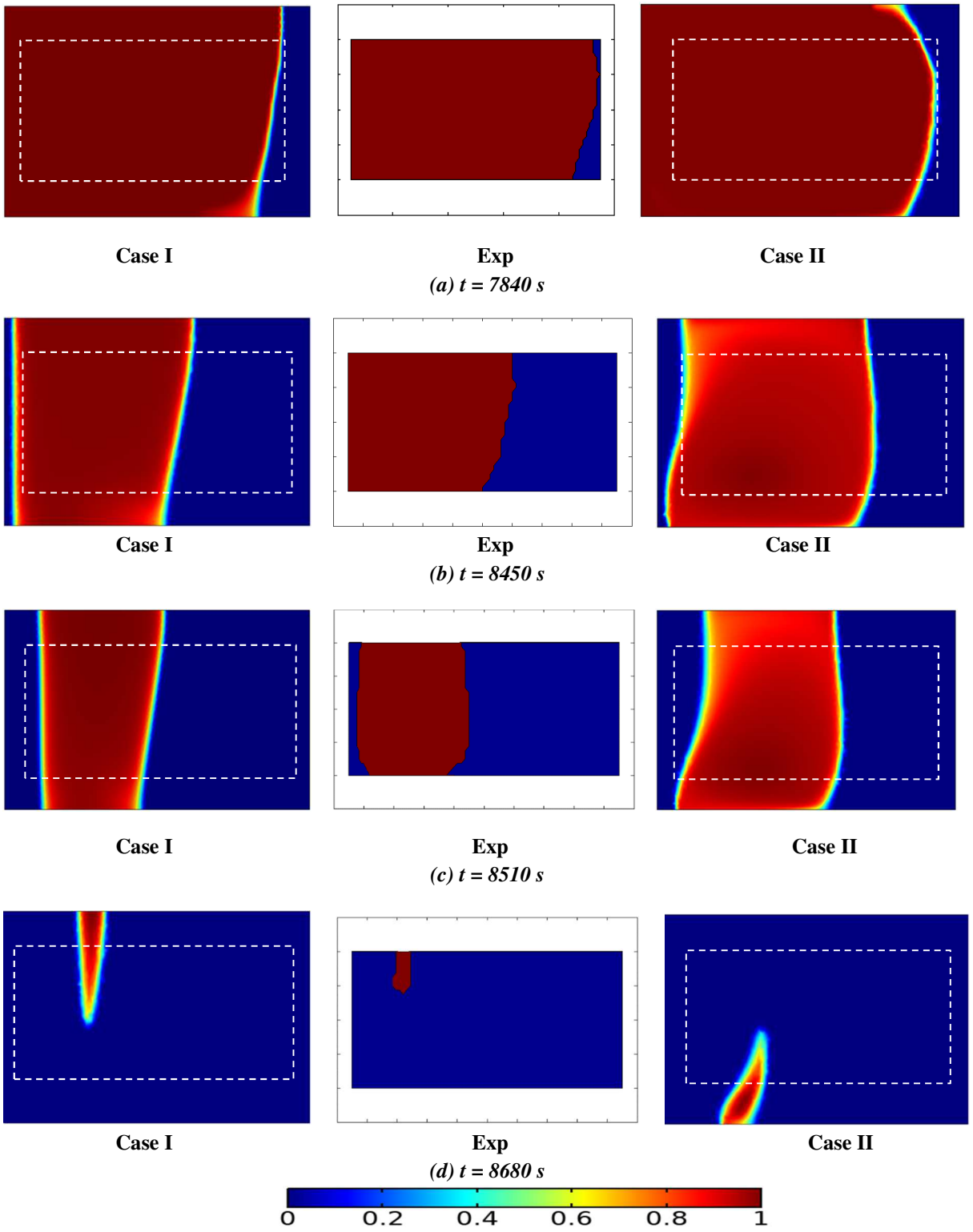

Fig. 14. Solid-liquid front positions at different times during the solidification process. Simulation results for natural convection (case I), experimental results for pure convection (Exp) and simulation results for forced convection (case II) are shown in the left, middle and the right columns, respectively. The colour bar gives the liquid fraction.

Conclusion:

A 3D solidification model, implemented in COMSOL software, is used to simulate the solidification of the pure material (tin) in a horizontal differentially heated rectangular cavity. The configuration is related to the AFRODITE solidification benchmark experimental setup. The experimental results are also available as temperature data recorded during the solidification phase, allowing comparison between numerical and experimental results. The solidification model has been derived on the basis of an enthalpy formulation based on fixed-grid techniques. With this model, very good agreements are obtained with the measured thermal fields and front progress during the solidification process. This implies that the buoyancy convection is correctly taken into account in the 3D simulation. The model used has also shown its effectiveness in predicting the process of tin solidification under forced convection generated by electromagnetic stirring in terms of velocity field, temperature field and morphology of the solidification front. The primary application of the EMS is to homogenize and control the temperature field during the stabilization stage (stage 2). However, EMS can be also used during solidification stages (stages 4 and 5 in Fig. 2). Our approach to calculating the interface temperature had shown good results to validate our model as obtained in Fig. 12.

Lastly, a full experimental solidification process run in the AFRODITE setup and its 3D numerical counterpart is reported. The experimental temperature data has been processed thoroughly to define appropriate unsteady thermal boundary conditions for the numerical model. Reasonable agreement is observed between the numerical and experimental results in terms of the evolution of the solid-liquid front positions over time, despite discrepancies in the shape of the fronts.

Looking forward, the application of EMS has demonstrated its effectiveness on the velocity and thermal fields through the homogenization of the temperature in the liquid bath. This offers the opportunity to apply this external electromagnetic force to alloys in order to avert defects due to segregation (concentration heterogeneity). Such defects are due to the effect of convection in the mushy zone.

Acknowledgments:

This work is a joint cooperation between the Materials physics Laboratory (LPM) of Amar Telidji University, Laghouat (Algeria), the SIMAP laboratory, Grenoble INP (France) and the Christian-Doppler Laboratory for Metallurgical Applications of Magnetohydrodynamics, Montanuniversitaet of Leoben, Franz-Josef-Str. 18, A-8700 Leoben, (Austria). The authors gratefully acknowledge financial support from The Ministry of Higher Education and Scientific Research of Algeria.

The SIMAP laboratory acknowledges the financial support provided by the ESA-MAP MICAST project contract 14347/01/NL/SH.

Abdellah Kharicha acknowledges financial support from the Austrian Federal Ministry of Economy, Family and Youth and the National Foundation for Research, Technology and

Development within the framework of the Christian-Doppler Laboratory for Metallurgical Applications of Magnetohydrodynamics.

Appendix A. Velocity field calculation

Table A.1

Time of passage of the solidification front recorded by each measurement point (10 thermocouples) (line located at mid-height of the sample). The table also gives the values of the velocity of the columnar front.

Nodes	Time of passage of the solidification front (s)	Estimation of the solidification front velocity $Vi = \Delta x / (Tag_{i+1} - Tag_i)$ in µm/s
L30	7900	$V_{30-29} = 45.45$
L29	8120	$V_{29-28} = 47.61$
L28	8330	$V_{28-27} = 57.14$
L27	8505	$V_{27-26} = 60.60$
L26	8670	$V_{26-25} = 83.33$
L25	8790	$V_{25-24} = 90.90$
L24	8900	$V_{24-23} = 95.23$
L23	9005	$V_{23-22} = 181.81$
L22	9060	$V_{22-21} = -250$
L21	9020	$V_{30-22} = 68.96$

- **Finite difference method**

This appendix provides details concerning the discretization of the heat equation in the liquid zone (without latent heat).

The controlling heat equation:

$$\frac{\partial T}{\partial t} + \vec{U}.\vec{\nabla}T = \alpha \nabla^2 T \ ,$$

where α is the thermal diffusivity of the pure tin.

The heat equation is discretized by means of the finite difference method centred in space and a second order leap-frog scheme in time.

$$\left[\frac{\partial T}{\partial t}\right]_{(i,j)} = \left(\frac{T(i,j,k) - T(i,j,k-\delta t)}{\delta t}\right)$$

$$\left[\vec{\nabla}T\right]_{(i,j)}^{k-\delta t/2} = \left[\left(\frac{T(i,j+1,k-\delta t/2) - T(i,j-1,k-\delta t/2)}{2\delta x}\right)\left(\frac{T(i+1,j,k-\delta t/2) - T(i-1,j,k-\delta t/2)}{2\delta y}\right)\right]$$

$$[\nabla^2 T]_{(i,j)}^{k-\delta t/2} = \left[\left(\frac{T(i,j+1,k-\delta t/2) + T(i,j-1,k-\delta t/2) - 2T(i,j,k-\delta t/2)}{2\delta x^2}\right)\left(\frac{T(i+1,j,k-\delta t/2) + T(i-1,j,k-\delta t/2) - 2T(i,j,k-\delta t/2)}{2\delta y^2}\right)\right]$$

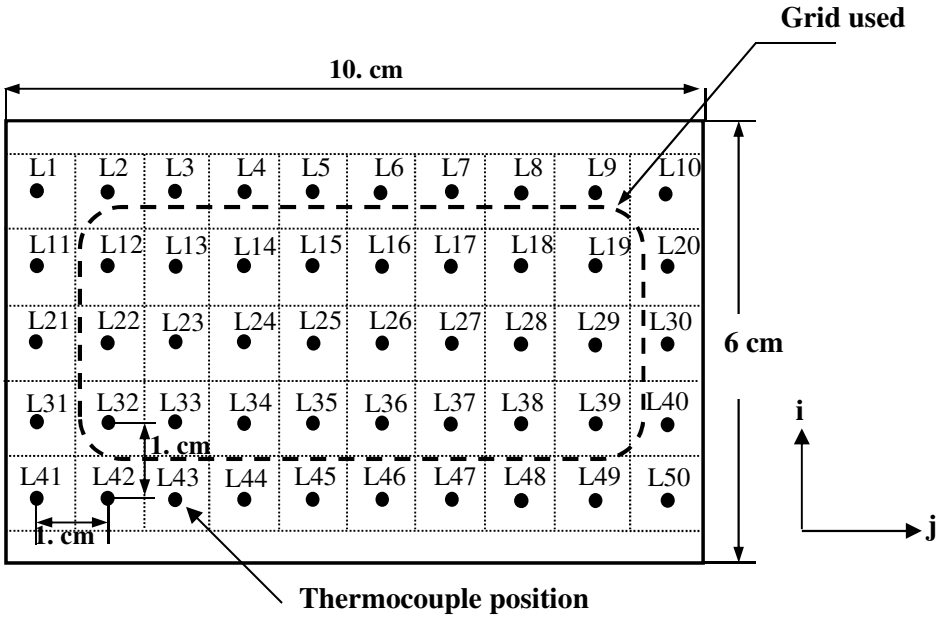

Fig. A. 1. Grid of points chosen for calculation of the field dynamic shown in the zone delimited by a discontinuous line.

Appendix B. Physical properties of the metal

Table B.1

Thermo-physical properties of pure tin

Property	Unit	Value	
Thermophysical data pure Sn			
Density, ρ	kg m^{-3}	7070	[35]
Coefficient of thermal expansion, β	K^{-1}	2.2e-5	[35]
Sn melting temperature, T_m	K	505	[35]
Enthalpy jump, *dH*	J kg^{-1}	59600	[35]
Solid metal heat capacity at constant pressure, *Cp1*	J/(kg.K)	200	[23]
Liquid metal heat capacity at constant pressure, *Cp2*	J/(kg.K)	318.81	[23]
Thermal conductivity, λ	W/ (m.K)	60	[35]
Dynamic viscosity, μ	Pa.s	0.00191	[35]
Kinematic viscosity, $\boldsymbol{\upsilon}$	m^2 s^{-1}	2.5e-7	[35]
Hot temperature, T_h	K	528	
Cold temperature, T_c	K	508	
Cooling rate, *CR*	K s^{-1}	0.03	
Electromagnetic forces, Eq.			
Electrical conductivity, $\boldsymbol{\sigma}$	$\Omega^{-1}m^{-1}$	3.4 x 10^6	[23]
Frequency, *f*	Hz	50	

- **The development of the electromagnetic force expressions**

The expression of the electromagnetic force $\boldsymbol{F = J \times B}$ was developed in reference [26], for a confined configuration identical to that of our case, as follows:

$$\begin{cases} F_x = \frac{\sigma\omega k^*}{2} A_0\, exp(-2k^*z) + \frac{k^* A_0^2}{2} exp(-2k^*z)\left[\left(\frac{\pi}{2e}\right)^2 \frac{sin(2X^*)}{\mu} - \sigma\omega\, cos(2X^*)\right] \\ F_y = -\frac{\pi k^* \beta^* A_0^2}{2\mu e} exp(-2k^*z)\, cos(2X^*) + \frac{\pi A_0^2}{4\mu e}\beta^{*2}\, exp(-2k^*z)\, sin(2X^*) \\ F_z = \frac{A_0^2}{2}\left[\sigma\omega\beta^* - \left(\frac{\pi}{2e}\right)^2 \frac{k^*}{\mu}\right] exp(-2k^*z) - \frac{A_0^2}{2}\left[\sigma\omega\beta^* - \left(\frac{\pi}{2e}\right)^2 \frac{k^*}{\mu}\right] exp(-2k^*z)\, cos(2X^*) \\ \quad - \frac{A_0^2}{2}\left[\sigma\omega\beta^* - \left(\frac{\pi}{2e}\right)^2 \frac{k^*}{\mu}\right] exp(-2k^*z)\, sin(2X^*) \end{cases} \quad \text{(B.1)}$$

with $X^* = k^*x - \frac{\pi y}{2e} + \beta^* z - \omega t$

Appendix C. Instantaneous temperature matrices

Table C.1

The instantaneous temperature matrices recorded for the case of experimental natural convection

Time (s)	Temperature distribution (K)									
7609	519.80	515.16	513.88	513.54	513.71	513.22	512.42	511.83	511.15	507.91
	519.75	516.90	515.96	515.65	515.76	515.53	514.76	514.57	513.82	510.51
	521.30	518.65	517.88	517.56	517.94	517.51	516.85	516.51	515.84	513.00
	524.56	521.25	519.69	519.27	519.22	518.99	518.22	517.80	516.37	512.33
	527.67	523.29	520.81	520.01	519.62	519.47	518.65	517.81	515.43	510.35
7897	515.15	511.51	510.39	510.12	510.38	510.04	509.19	508.09	505.23	500.00
	515.11	512.75	512.01	511.64	511.84	511.68	510.81	510.06	506.89	501.56
	516.30	514.07	513.41	513.12	513.47	513.06	512.31	511.55	508.99	503.81
	518.73	516.14	514.80	514.44	514.40	514.19	513.36	512.64	510.06	504.30
	521.06	517.68	515.56	514.83	514.46	514.33	513.46	512.48	509.42	503.24
8735	504.49	505.13	505.19	505.60	504.14	500.49	496.07	491.31	486.59	479.31
	504.98	505.28	505.47	505.43	504.50	501.31	496.83	492.70	487.82	481.18
	505.11	505.19	505.42	505.45	504.98	501.98	497.74	493.49	488.86	482.70
	505.02	505.64	505.43	505.39	504.86	502.50	498.55	494.32	489.26	482.76
	504.42	505.47	505.18	504.88	504.13	502.41	499.01	494.85	490.31	485.21

Appendix D. Thermal flux estimation method, based on complete quadratic element

This method uses a one-dimensional Lagrangian quadratic approximation in both directions ξ and η.

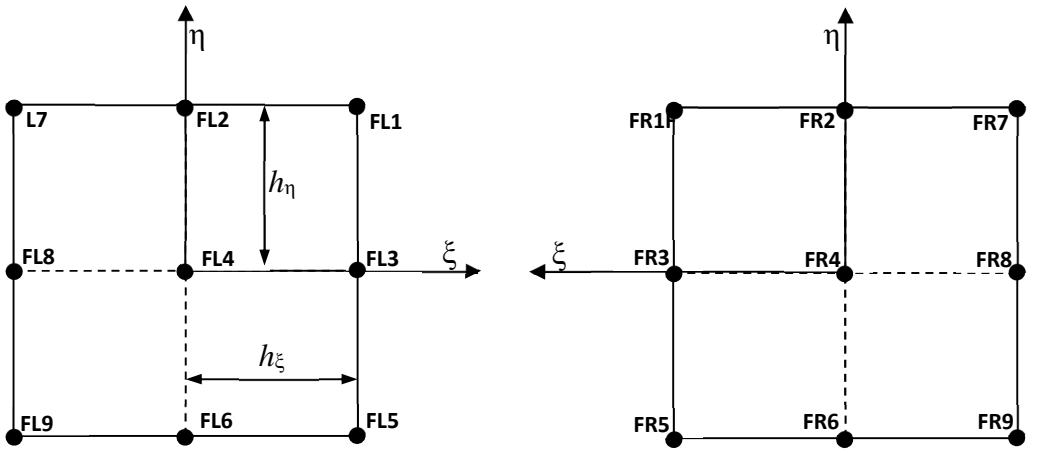

Fig. D1. Diagram illustrating the distribution of the thermocouples of each exchanger on a complete quadratic element.

- **Interpolation functions**

{N}	$\{\partial N/\partial \xi\}$
FR1	$\frac{(1+2\xi)(1+\eta)\eta}{4}$
FR2	$-(1+\eta)\,\xi\,\eta$
FR3	$\frac{(1+2\xi)(1-\eta^2)}{2}$
FR4	$-2(1-\eta^2)\,\xi$
FR5	$\frac{-(1+2\xi)(1-\eta)\eta}{4}$
FR6	$(1-\eta)\,\xi\,\eta$
FR7	$\frac{-(1-2\xi)(1+\eta)\eta}{4}$
FR8	$\frac{-(1-2\xi)(1-\eta^2)}{2}$
FR9	$\frac{(1-2\xi)(1-\eta)\eta}{4}$

- **Application of the method**

It interpolates the temperature field using the functions Nn (x, y) defined previously:

$$T(x,y,t) = \sum_{n=1}^{9} N_n(x,y).T_n(t) \quad \text{(D.1)}$$

Or:

$$\lambda.\left(\frac{\partial T}{\partial x}\right)_{\Gamma} = \lambda.\sum_{n=1}^{9} T_n(t)\left(\frac{\partial N_n(x,y)}{\partial x}\right) \quad \text{(D.2)}$$

Γ : the exchange surface

- **Integration method on complete quadratic element**

In the exchange surface $\xi = 1$ and η [-1 ; +1]

$$\lambda.s.\left(\frac{\partial T}{\partial x}\right)_{\Gamma} = \frac{\lambda.s}{h_{\xi}}\int_{-1}^{+1}\left[\left(\frac{(1+2\xi)(1+\eta)\eta}{4}\right)FR1(t) + (-(1+\ \eta)\xi\ .\eta)FR2(t) + \left(\frac{(1+2\xi)(1-\eta^2)}{2}\right)FR3(t) + (-2(1-\ \eta^2)\ \xi)FR4(t) + \left(\frac{-(1+2\xi)(1-\eta)\eta}{4}\right)FR5(t) + ((1-\ \eta)\ \xi\ \eta)FR6(t) + \left(\frac{-(1-2\xi)(1+\eta)\eta}{4}\right)FR7(t) + \left(\frac{-(1-2\xi)(1-\eta^2)}{2}\right)FR8(t) + \left(\frac{(1-2\xi)(1-\eta)\eta}{4}\right)FR9(t)\right]_{\xi=1} d\eta \quad \text{(D.3)}$$

$$\lambda.s.\left(\frac{\partial T}{\partial x}\right)_{\Gamma} = \frac{\lambda.s}{h_{\xi}}\int_{-1}^{+1}\left[\left(\frac{3(1+\eta)\eta}{4}\right)FR1(t) + (-(1+\ \eta)\ .\eta)FR2(t) + \left(\frac{3(1-\eta^2)}{2}\right)FR3(t) + (-2(1-\ \eta^2)\ )FR4(t) + \left(\frac{-3(1-\eta)\eta}{4}\right)FR5(t) + ((1-\ \eta)\ \eta)FR6(t) + \left(\frac{(1+\eta)\eta}{4}\right)FR7(t) + \left(\frac{(1-\eta^2)}{2}\right)FR8(t) + \left(\frac{-(1-\eta)\eta}{4}\right)FR9(t)\right]_{\xi=1} d\eta \quad \text{(D.4)}$$

$$\lambda.s.\left(\frac{\partial T}{\partial x}\right)_{\Gamma} = \frac{\lambda.s}{h_{\xi}}\left[\left(\frac{3}{8}\eta^2 + \frac{3}{12}\eta^3\right)FR1(t) - \left(\frac{1}{2}\eta^2 + \frac{1}{3}\eta^3\ \right)FR2(t) + \left(\frac{3}{2}\eta - \frac{1}{2}\eta^3\right)FR3(t)\left(-2\eta + \frac{2}{3}\ \eta^3\right)\right)FR4(t) + \left(-\frac{3}{8}\eta^2 + \frac{3}{12}\eta^3\right)FR5(t) + \left(\frac{1}{2}\eta^2 - \frac{1}{3}\eta^3\ \right)FR6(t) + \left(\frac{1}{8}\eta^2 + \frac{1}{12}\eta^3\right)FR7(t) + \left(\frac{1}{2}\eta - \frac{1}{6}\eta^3\right)FR8(t) + \left(-\frac{1}{8}\eta^2 + \frac{1}{12}\eta^3\right)FR9(t)\right]_{-1}^{+1} \quad \text{(D.5)}$$

$$\lambda.s.\left(\frac{\partial T}{\partial x}\right)_{\Gamma} = \frac{\lambda.s}{h_{\xi}}\left(\frac{FR1(t)}{2} - \frac{2}{3}FR2(t) + 2FR3(t) - \frac{8}{3}FR4(t) + \frac{1}{2}FR5(t) - \frac{2}{3}FR6(t) + \frac{1}{6}FR7(t) + \frac{2}{3}FR8(t) + \frac{1}{6}FR9(t)\right) \quad \text{(D.6)}$$

- **Heat flow on the right side**

$$\phi_R(t) = \frac{\lambda.s}{h_\xi}\left(-\frac{FR1(t)}{2} + \frac{2}{3}FR2(t) - 2FR3(t) + \frac{8}{3}FR4(t) - \frac{1}{2}FR5(t) + \frac{2}{3}FR6(t) - \frac{1}{6}FR7(t) - \frac{2}{3}FR8(t) - \frac{1}{6}FR9(t)\right) \quad \text{(D.7)}$$

- **Heat flow on the left side**

$$\phi_L(t) = \frac{\lambda.s}{h_\xi}\left(\frac{FL1(t)}{2} - \frac{2}{3}FL2(t) + 2FL3(t) - \frac{8}{3}FL4(t) + \frac{1}{2}FL5(t) - \frac{2}{3}FL6(t) + \frac{1}{6}FL7(t) + \frac{2}{3}FL8(t) + \frac{1}{6}FL9(t)\right) \quad \text{(D.8)}$$

Where λ_{Cu} is the thermal conductivity of copper $(\lambda_{Cu} = 386W.m^{-1}.K^{-1})$, S the heat exchange surface $(S = 6.10^{-4}m^2)$ and h_ξ is the step in the horizontal direction $\left(h_\xi = 15mm\right)$. (FL1, FL2, ...FL9) and (FR1, FR2, ..., FR9) are the thermocouples of the left and right exchanger respectively.

References

[1] Hebditch, D. and J. Hunt, *Observations of ingot macrosegregation on model systems.* Metallurgical and Materials Transactions B, 1974. **5**(7): p. 1557-1564.

[2] M. Bellet, H. Combeau, Y. Fautrelle, D. Gobin, M. Rady, E. Arquis, O. Budenkova, B. Dussoubs, Y. Duterrail, A. Kumar, C.A. Gandin, B. Goyeau, S. Mosbah, M. Zaloznik, *Call for contributions to a numerical benchmark problem for 2D columnar solidification of binary alloys.* International Journal of Thermal Sciences, 2009. **48**(11): p. 2013-2016.

[3] N. Ahmad, H. Combeau, J.-L. Desbiolles, T. Jalanti, G. Lesoult, J. Rappaz, M. Rappaz and C. Stomp, *Numerical simulation of macrosegregation: a comparison between finite volume method and finite element method predictions and a confrontation with experiments.* Metallurgical and Materials Transactions A, 1998. **29**(2): p. 617-630.

[4] Schneider, M.C. and C. Beckermann, *A numerical study of the combined effects of microsegregation, mushy zone permeability and fllow, caused by volume contraction and thermosolutal convection, on macrosegregation and eutectic formation in binary alloy solidification.* International Journal of Heat and Mass Transfer, 1995. **38**(18): p. 3455-3473.

[5] L. Hachani, K. Zaidat and Y. Fautrelle, *Multiscale statistical analysis of the tin-lead alloy solidification process*, Int. J. Thermal Sciences, 110 (2016) 186-205.

[6] X. Wang, P. Petitpas, C. Garnier, J. P. Paulin and Y. Fautrelle, *A quasi two-dimensional benchmark experiment for the solidification of a tin-lead binary alloy*, C. R. Mecanique, 335 (2007) 336-341.

[7] X. Wang and Y. Fautrelle, *an investigation of the influence of natural convection on tin solidification using a quasi-two-dimensional experimental benchmark*, Int. J. Heat Mass Transfer, 52 (2009) 5624-5633.

[8] L. Hachani, B. Saadi, X. Wang, A. Nouri, K. Zaidat, A. Belgacem-Bouzida, L. Ayouni-Derouiche, G. Raimondi and Y. Fautrelle, *Experimental analysis of the solidification of Sn-3 wt%Pb alloy under natural convection,* Int. J. Heat Mass Transfer, 55 (2012) 1986-1996.

[9] R. Boussaa, O. Budenkova, L. Hachani, X. D. Wang, B. Saadi, K. Zaidat, H. Ben Hadid and Y. Fautrelle, in: *CFD Modeling and Simulation in Materials Processing*, John Wiley & Sons, Inc., Hoboken, NJ, USA, (2012) 163-170.

[10] R. Boussaa, L. Hachani, O. Budenkova, V. Botton, D. Henry, K. Zaidat, H. Ben Hadid and Y. Fautrelle, Macrosegregations in Sn-3 wt%Pb alloy solidification: *Experimental and 3D numerical simulation investigations*, Int. J. Heat Mass Transfer, 100 (2016) 680-690.

[11] A. K. Haagen, E. Franquet, E. Pernot and D. Brüggemann, *A comprehensive benchmark of fixedgrid methods for the modeling of melting*, International Journal of Thermal Sciences, 118 (2017) 69-103.

[12] E. Franquet, A. K. Haagen and D. Brüggemann, *On the modeling impacts of the energy equation in the simulation of melting, invited talk*, Coupled problems conference 2017, VII International Conference on Coupled Problems in Science and Engineering, Rhodes Island, Greece, 12-14 June 2017.

[13] V. Botton, R. Boussaa, R. Debacque, L. Hachani, K. Zaidat, H. Ben Hadid, Y. Fautrelle and D. Henry, *A 2D model for low Prandtl number convection in an enclosure*, Int. J. Thermal Sciences, 71 (2013) 53-60.

[14] C. Bonacina, G. Comini, A. Fasano, and M. Primicerio, Numerical Solution of Phase- Change Problems, Int. J. Heat Mass Transfer, vol. 16, pp. 1825-1832, 1973.

[15] T. Campanella, C. Charbon, M. Rappaz, Grain refinement induced by electromagnetic stirring: a dendrite fragmentation criterion, Metall. Mater. Trans. A 35 (10) (2004) 3201–3210.

[16] Z. Yang, P.K. Seo, C.G. Kang, Grain size control of semisolid A356 alloy manufactured by electromagnetic stirring, J. Mater. Sci. Technol. 21 (2) (2005) 219–225.

[17] Li Xi, Y. Fautrelle, Z.M. Ren, Influence of thermoelectric effects on the solid– liquid interface shape and cellular morphology in the mushy zone during the directional solidification of Al–Cu alloys under a magnetic field, Acta Mater. 55 (11) (2007) 3803–3813.

[18] X. Meng, C. Chen, Z. Hong, J. Wang, Effect of rotating magnetic field on the solidification structures of Pb–Sn alloys, Sci. China Ser. E 49 (3) (2006) 274– 282.

[19] K. Zaïdat, N. Mangelinck-Noël, R. Moreau, Control of melt convection by a traveling magnetic field during the directional solidification of Al–Ni alloys, C. R. Méc. 335 (5–6) (2007) 330–335.

[20] D. Samanta, N. Zabaras, Control of macrosegregation during the solidification of alloys using magnetic fields, Int. J. Heat Mass Transfer 49 (25–26) (2006) 4850–4866.

[21] W.C. Johnston, G.R. Kotler, W.A. Tiller, The influence of electromagnetic stirring on the nucleation of tin and tin–lead alloy, Trans. Metall. Soc. AIME 227 (4) (1963) 890–896.

[22] W.C. Johnston, G.R. Kotler, W.A. Tiller, Grain refinement via electromagnetic stirring during solidification, Trans. Metall. Soc. AIME 233 (9) (1965) 1856– 1960.

[23] L. Hachani, "Etude de l'influence de la convection naturelle et forcée sur le processus de la solidification: cas d'un alliage métallique binaire," Phd Materials, mechanics, civil engineering, electrochemistry, cotutelle between Grenoble and Laghouat University.

[24] R. Berton, "*Magnéto-hydrodynamique*", Masson, 1991.

[25] R. Moreau, "*The fundamental of MHD Related to crystal Growth*", Progress in crystal growth and characterization of materials, (1999), P.161.

[26] X.D. Wang, Y. Fautrelle, J. Etay, and R. Moreau: Metall. Mater. Trans. B, (2009), pp. 104-113.

[27] Robynne E. Murray and Dominic Groulx, Modeling convection during melting of a phase change material, In Proceedings of the COMSOL Conference, 2011.

[28] F. Wolf, R. Viskanta, Solidification of a pure metal at a vertical wall in the presence of liquid superheat, Int. J. Heat Mass Transf. 31 (1988) 1735–1744.

[29] M.H. Avnaim, A. Levy, B. Mikhailovich, O. Ben-David, A. Azulay, Comparison of three-dimensional multidomain and single-domain models for the horizontal solidification problem, J. Heat Transfer 138 (2016) 112301.

[30] M.H. Avnaim, B. Mikhailovich, A. Azulay, A. Levy, Numerical and experimental study of the traveling magnetic field effect on the horizontal solidification in a rectangular cavity. Part 2: acting forces ratio and solidification parameters, Int. J. Heat Fluid Flow 69 (2018) 9–22.

[31] Aina Rakotondrandisa, Georges Sadaka, Ionut Danaila. A finite-element toolbox for the simulation of solid-liquid phase-change systems with natural convection. Computer Physics Communications, 2020.

[32] Farid Samara, Dominic Groulx, and Pascal H. Biwole. Natural convection driven melting of phase change material: comparison of two methods. In Excerpt from the Proceedings of the COMSOL Conference, 2012.

[33] Robynne E. Murray and Dominic Groulx. Modeling convection during melting of a phase change material. In Proceedings of the COMSOL Conference, 2011.

[34] E. V. Rozhitsina, S. Gruner, I. Kaban, W. Hoyer, V. E. Sidorov, and P. S. Popel, Dynamic Viscosities of Pure Tin and Sn–Ag, Sn–Cu, and Sn–Ag–Cu Eutectic Melts, Russian Metallurgy (Metally), 2 (2011), 118–121.

[35] I. Hamzaoui, S. Millet, V. Botton, A. Benzaoui, D. Henry, L. Hachani, R. Boussaa, K. Zaidat, Y. Fautrelle, *A $2D^{1/2}$ model for natural convection and solidification in a narrow enclosure*, International Journal of Thermal Sciences, 140 (2019) 167-183.